DEVELOPMENT OF OXALATE CEMENTS WITH DEAD-BURNED MAGNESIA AND CALCIUM SULFOALUMINATE CLINKER

A THESIS SUBMITTED TO
THE GRADUATE SCHOOL OF NATURAL AND APPLIED SCIENCES
OF
MIDDLE EAST TECHNICAL UNIVERSITY

BY

SAİD BATUHAN BİLMEZ

IN PARTIAL FULFILLMENT OF THE REQUIREMENTS
FOR
THE DEGREE OF MASTER OF SCIENCE
IN
CIVIL ENGINEERING

JANUARY 2023

Approval of the thesis:

DEVELOPMENT OF OXALATE CEMENTS WITH DEAD-BURNED MAGNESIA AND CALCIUM SULFOALUMINATE CLINKER

submitted by **SAİD BATUHAN BİLMEZ** in partial fulfillment of the requirements for the degree of **Master of Science** i**n Civil Engineering, Middle East Technical University** by,

Prof. Dr. Halil Kalıpçılar
Dean, Graduate School of **Natural and Applied Sciences** _____

Prof. Dr. Erdem Canbay
Head of the Department, **Civil Engineering** _____

Prof. Dr. Sinan Turhan Erdoğan
Supervisor, **Civil Engineering, METU** _____

Examining Committee Members:

Prof. Dr. İsmail Özgür Yaman
Civil Engineering, METU _____

Prof. Dr. Sinan Turhan Erdoğan
Civil Engineering, METU _____

Assoc. Prof. Dr. Çağla Meral Akgül
Civil Engineering, METU _____

Assoc. Prof. Dr. Hande Işık Öztürk
Civil Engineering, METU _____

Asst. Prof. Dr. Seda Selçuk
Civil Engineering, Çankaya University _____

Date: 25.01.2023

I hereby declare that all information in this document has been obtained and presented in accordance with academic rules and ethical conduct. I also declare that, as required by these rules and conduct, I have fully cited and referenced all material and results that are not original to this work.

Name, Last name : Said Batuhan Bilmez

Signature :

ABSTRACT

DEVELOPMENT OF OXALATE CEMENTS WITH DEAD-BURNED MAGNESIA AND CALCIUM SULFOALUMINATE CLINKER

Bilmez, Said Batuhan
Master of Science, Civil Engineering
Supervisor : Prof. Dr. Sinan Turhan Erdoğan

January 2023, 75 pages

An emerging alternative to Portland cement, oxalate cement is a promising candidate for reducing the carbon footprint of the construction industry. Oxalic acid (OA) can be produced via direct electrochemical CO_2 reduction, making carbon-neutral cement with OA possible. This study investigates the development of the mechanical, mineralogical, and microstructural properties of clay oxalate cement (COC) made with OA salt and dead-burned magnesia (DBM). Methods to prepare clay oxalate (CO), the OA salt used in this study, and to produce COC mixtures are proposed. Calcium sulfoaluminate ($C\overline{S}A$) clinker was substituted for DBM to further lower the carbon footprint of COC mixtures. 28-day strengths of ~35 MPa were achieved in COC mortars with DBM, while those incorporating $C\overline{S}A$ reached ~30 MPa. The setting times of COC mixtures varied between 4 and 29 minutes. Mortars incorporating $C\overline{S}A$ set more rapidly than those with DBM. The reaction mechanism of COC pastes was studied using x-ray diffraction, pH measurement, thermogravimetric analysis, scanning electron microscopy, and mercury intrusion porosimetry. A magnesium oxalate hydrate, glushinskite, was observed inside the mostly amorphous medium of hydrated COC paste with DBM. COC mixtures containing DBM were more water resistant than the samples made only with $C\overline{S}A$

clinker. The findings of this study and simple calculations suggest that hybrid COC mixtures containing equal amounts of DBM and $C\bar{S}A$ (CO/DBM/$C\bar{S}A$=7.40/1.30/1.30, by mass) can provide medium strength, show sufficient resistance to water, as well as being carbon-neutral.

Keywords: oxalate cement, carbon-neutral, magnesium, calcium sulfoaluminate

ÖZ

ÖLÜ YANMIŞ MAGNEZYA VE KALSİYUM SÜLFOALUMİNAT KLİNKERİ İLE OKSALAT ÇİMENTOLARININ GELİŞTİRİLMESİ

Bilmez, Said Batuhan
Yüksek Lisans, İnşaat Mühendisliği
Tez Yöneticisi: Prof. Dr. Sinan Turhan Erdoğan

Ocak 2023, 75 sayfa

Portland çimentosuna yeni bir alternatif olan oksalat çimentosu, inşaat sektörünün karbon ayak izini azaltmak için umut verici bir adaydır. Oksalik asit (OA), doğrudan elektrokimyasal CO_2 indirgemesi yoluyla üretilebilir ve bu da OA ile karbon-nötr çimentoyu mümkün kılar. Bu çalışma, OA tuzu ve ölü yanmış magnezya (ÖYM) ile yapılan kil oksalat çimentosunun (KOÇ) mekanik, mineralojik ve mikroyapısal özelliklerinin gelişimini araştırmaktadır. Bu çalışmada kullanılan OA tuzu olan kil oksalatın (KO) hazırlanması ve KOÇ karışımlarının üretilmesi için yöntemler önerilmiştir. KOÇ karışımlarının karbon ayak izini daha da azaltmak için ÖYM yerine kalsiyum sülfoalüminat ($K\overline{S}A$) klinkeri kullanılmıştır. ÖYM içeren KOÇ harçlarında ~35 MPa'lık 28 günlük dayanım elde edilirken, $K\overline{S}A$ içerenler ~30 MPa'ya ulaşmıştır. KOÇ karışımlarının priz süreleri 4 ila 29 dakika arasında değişmiştir. $K\overline{S}A$ içeren harçlar ÖYM içerenlere göre daha hızlı priz almıştır. KOÇ hamurlarının reaksiyon mekanizması x-ışını kırınımı, pH ölçümü, termogravimetrik analiz, taramalı elektron mikroskobu ve cıva intrüzyon porozimetrisi kullanılarak incelenmiştir. Hidratlanmış ÖYM'li KOÇ hamurunun çoğunlukla amorf ortamında bir magnezyum oksalat hidratı olan glushinskite gözlenmiştir. ÖYM içeren KOÇ

karışımları, sadece K$\overline{S}$A klinkeri ile yapılan numunelere göre suya daha dayanıklıdır. Bu çalışmanın bulguları ve basit hesaplamalar, eşit miktarda ÖYM ve K$\overline{S}$A içeren hibrit KOÇ karışımlarının (KO/ÖYM/K$\overline{S}$A = 7.40/1.30/1.30, kütlece) orta dayanım sağlayabileceğini, suya karşı yeterli direnç gösterebileceğini ve karbon-nötr olduğunu göstermektedir.

Anahtar Kelimeler: oksalat çimentosu, karbon-nötr, magnezyum, kalsiyum sülfoaluminat

Dedicated to the sunny days ahead

ACKNOWLEDGMENTS

Words cannot express my gratitude to my supervisor Prof. Sinan Turhan Erdoğan, for his guidance, encouragement, and patience since my undergraduate years. Whenever I ran out of motivation, he was always there to refill the tank and help me move on. I will always be thankful to him for teaching me a lot about science and life.

I would like to thank my friend Baki Aykut Bilginer without whom working in the laboratory would not be as easy as it was. I will be forever indebted to him for his support and friendship throughout my study.

Many thanks to everyone in the Construction Materials Laboratory of METU for their friendship and assistance.

I want to acknowledge Demireller Mining Inc. for their help in procuring the bauxite used in this study.

I would be remiss if I did not mention the fellowship of CEITECH for broadening my horizons and the inspiration they gave me.

Last but not least, I could not have undertaken this journey without the invaluable support of my beloved family and my one and only, Seval. My biggest purpose has been and will always be to make them proud.

TABLE OF CONTENTS

ABSTRACT v

ÖZ vii

ACKNOWLEDGMENTS x

TABLE OF CONTENTS xi

LIST OF TABLES xv

LIST OF FIGURES xvi

LIST OF ABBREVIATIONS xix

CHAPTERS

1 INTRODUCTION 1

1.1 Research Background 1

1.2 Objectives and Scope 2

2 LITERATURE REVIEW 5

2.1 Introduction 5

2.2 Acid-Base Cements 5

2.2.1 General Information 5

2.2.2 Reaction Mechanism 6

2.3 Oxalic Acid and Oxalate Cements 7

2.3.1 General Information 7

2.3.2 Oxalate Cements 9

2.4 Magnesia 14

2.4.1 General Information 14

2.4.2 Magnesium Phosphate Cement 16

2.5 Calcium Sulfoaluminate Cement 20
2.5.1 General Information 20
2.5.2 Hydration Mechanism 21
3 EXPERIMENTAL PROCEDURE 23
3.1 Materials 23
3.1.1 Oxalic Acid 23
3.1.2 Clay 23
3.1.3 Dead-burned Magnesia 25
3.1.4 Raw Materials Used in C$\overline{S}$A Clinker Production 26
3.2 Methods 27
3.2.1 Production of Clay Oxalate 27
3.2.2 Production of C$\overline{S}$A Clinker 29
3.2.3 Preparation of Clay Oxalate Cement with DBM and C$\overline{S}$A 30
3.2.4 Calculation of Carbon-Neutral COC Mix Proportions 32
3.3 Experiments 32
3.3.1 Compressive Strength 32
3.3.2 X-ray Diffraction Analysis 33
3.3.3 pH Measurement 34
3.3.4 Setting Time 34
3.3.5 Thermogravimetric Analysis – Differential Scanning Calorimetry 35
3.3.6 Scanning Electron Microscopy 35
3.3.7 Mercury Intrusion Porosimetry 35
3.3.8 Coffee Cup Temperature Measurement 36
3.3.9 Water Resistance 37

4 RESULTS AND DISCUSSION 39
4.1 Determination of S/B in COC Mortars 39
4.2 Compressive Strength 40
4.2.1 Influence of W/B on the Compressive Strength of MCO Mortars.....40
4.2.2 Influence of CO/DBM on the Compressive Strength of MCO Mortars ...41
4.2.3 Influence of CO/C$\bar{S}$A on the Compressive Strength of C$\bar{S}$ACO Mortars 42
4.2.4 Influence of C$\bar{S}$A Clinker Replacement on the Compressive Strength of COC Mortars.....42
4.3 X-ray Diffraction Analysis 45
4.3.1 Influence of C/OA on the Crystal Structure of CO 45
4.3.2 Influence of Calcination on the Crystal Structure of Magnesia 46
4.3.3 Influence of the Change in CO/DBM Ratio on the Crystal Structure of MCO Pastes with Age.....47
4.3.4 Influence of Replacing DBM with C$\bar{S}$A Clinker on the Crystal Structure of COC Pastes 48
4.4 Setting Time.....49
4.5 pH Measurement.....51
4.6 Thermogravimetric Analysis 52
4.7 Scanning Electron Microscopy 57
4.8 Mercury Intrusion Porosimetry.....59
4.9 Coffee Cup Temperature Measurement.....61
4.10 Water Resistance.....62
4.11 Carbon Footprint Analysis for Optimal COC Mix Proportions.....64
4.11.1 Optimal Mix Proportion Calculation for MCO Paste 64
4.11.2 Optimal Mix Proportion Calculation for HYBCO Paste 65

4.11.3 Optimal Mix Proportion Calculation for C$\overline{S}$ACO Paste 65
5 CONCLUSIONS AND RECOMMENDATIONS 67
5.1 Conclusions 67
5.2 Recommendations for Future Studies 68
REFERENCES 69

LIST OF TABLES

TABLES

Table 2.1 Energy requirement and CO_2 released during the formation of cement compounds. Adapted from Sharp et al. (1999). 21
Table 3.1 The oxide composition and the LOI of the clay used. 23
Table 3.2 The oxide compositions of raw materials used in CSA clinker production. 26
Table 3.3 C/OA used in the preliminary works to produce CO. 28
Table 3.4 Sample calculation of raw materials proportion to produce 1 kg of CSA clinker. 30
Table 3.5 Mixture proportions used in compressive strength tests. 33
Table 4.1 Setting times of COC mortars. 51
Table 4.2 CO_2 emission data of the materials used in the preparation of COC mixtures. 64

LIST OF FIGURES

FIGURES

Figure 2.1 The stages of the formation of an acid-base cement (Wagh, 2016). 6
Figure 2.2 Six primary feedstocks by which oxalic acid is produced: (a) CO2, (b) CO, (c) alkali formate, (d) ethylene glycol, (e) propylene, and (f) carbohydrates (Schuler et al., 2021). 8
Figure 2.3 (a) Strength development of MgOx mortars, and (b) temperature evolution of MgOx pastes and PC. (Erdoğan et al., 2022). 11
Figure 2.4 (a) Compressive strength and setting time of FOC paste specimens with changing CS/OA, and (b) XRD patterns of FOC paste with CS/OA = 3.6 (Luo et al., 2021). 13
Figure 2.5 Flow diagram of the wet method (Shand et al., 2020). 16
Figure 2.6 (a) The change in pH with time after adding MgO to an H_3PO_4 solution (Wagh & Jeong, 2003), and (b) the change in setting times of MPCs with M/P (Shand et al., 2020). 17
Figure 2.7 (a) Images of MPC pastes with increasing borax content from top to bottom, and (b-c) initial and final setting times of MPC pastes. (Gelli et al., 2022). 18
Figure 2.8 The effect of increasing the borax-to-magnesia ratio (from 2.5 % (mix 1) to 12.5 % (mix 5) by 2.5 % increments) on the strength of MKPC pastes. (Yang & Qian, 2010). 19
Figure 2.9 Comparison of the pH of MAPC (solid curves) and MKPC (dotted curve) (Le Rouzic et al., 2017). 20
Figure 2.10 XRD patterns of C$\overline{S}$A clinker and hydrated C$\overline{S}$A cement at 1, 3, and 28 days of hydration (Canbek, 2018). 22
Figure 3.1 XRD pattern of the clay used. (Q: quartz, Mt: montmorillonite) 24
Figure 3.2 The effect of calcination on the specific gravity of magnesia (Bilginer, 2018). 25

Figure 3.3 XRD pattern of C$\overline{S}$A clinker prepared. (Br: brownmillerite, Y: ye'elimite, Be: belite)..... 27
Figure 3.4 (a) CO after mixing and (b) CO after oven drying. The container in the pictures is 30 cm in length, 25 cm in width, and 5 cm in depth..... 29
Figure 3.5 C$\overline{S}$A clinker paste shaped as slender sticks and ordered in a grid pattern. 30
Figure 3.6 (a) The experimental setup for temperature measurement. The data logger is in the middle, and the cups with the COC pastes inside. (b) Close-up of a measurement cup showing the thermocouple wire and mixing hole plug. 37
Figure 3.7 The experimental setup for water resistance testing. 5-cm COC mortar cube specimens are underwater..... 38
Figure 4.1 Visual change in the surface texture of 5-cm cubic mortar specimens for S/B of (a) 2.50, (b) 2.75, and (c) 3.00. 39
Figure 4.2 The change in compressive strength of CO7-DBM for changing W/B. Error bars show the standard deviation in strength. 40
Figure 4.3 The change in the compressive strength of MCO specimens with varying CO/DBM. Error bars show the standard deviation in strength. 41
Figure 4.4 The change in the compressive strength of C$\overline{S}$ACO specimens with varying CO/C$\overline{S}$A. Error bars show the standard deviation in strength. 42
Figure 4.5 The strength development of the COC mortars of CO6-DBM, CO6-HYB, and CO6-C$\overline{S}$A. Error bars show the standard deviation in strength. 43
Figure 4.6 The strength development of the COC mortars of CO7-DBM, CO7-HYB, and CO7-C$\overline{S}$A. Error bars show the standard deviation in strength. 44
Figure 4.7 The strength development of the COC mortars of CO8-DBM, CO8-HYB, and CO8-C$\overline{S}$A. Error bars show the standard deviation in strength. 45
Figure 4.8 The XRD patterns observed in CO-1.50, CO-1.00, and CO-0.67. (Q: quartz, Wd: weddellite, X: oxalic acid) 46
Figure 4.9 The XRD patterns observed in uncalcined MgO and DBM. (P: periclase, M: magnesite, F: forsterite)..... 47

Figure 4.10 The XRD patterns of CO3-DBM, CO5-DBM, and CO7-DBM pastes at 1d, 7d, and 28d. (G: glushinskite, Q: quartz, P: periclase) 48
Figure 4.11 The XRD patterns of CO7-DBM, CO7-HYB, and CO7-C$\overline{S}$A pastes at the ages of 1, 7, and 28 days. (G: glushinskite, Q: quartz, P: periclase, Y: ye'elimite, E: ettringite) 49
Figure 4.12 Penetration depth of Vicat needle for various COC mortars. 50
Figure 4.13 pH measurement results for COC pastes prepared with CO7-DBM, CO7-HYB, and CO7-C$\overline{S}$A. 52
Figure 4.14 Thermogravimetric analysis of CO7-DBM, CO7-HYB, and CO7-C$\overline{S}$A pastes at 1d. 54
Figure 4.15 Thermogravimetric analysis of CO7-DBM, CO7-HYB, and CO7-C$\overline{S}$A pastes at 28d. 56
Figure 4.16 SEM images of CO7-DBM pastes at (a-b) 1d and (c-d) 28d. 57
Figure 4.17 SEM images of CO7-HYB pastes at (a-b) 1 day and (c-d) 28 days. ... 58
Figure 4.18 SEM images of CO7-C$\overline{S}$A pastes at (a-b) 1 day, and (c-d) 28 day..... 59
Figure 4.19 (a) Cumulative porosity and (b) pore size distribution of CO7-DBM, CO7-HYB, and CO7-C$\overline{S}$A pastes..... 60
Figure 4.20 Coffee cup temperature measurement for COC pastes. 62
Figure 4.21 The change in compressive strength of CO7-DBM, CO7-HYB, and CO7-C$\overline{S}$A mortar specimens after immersed in water for 1, 7, and 28 days. 63

LIST OF ABBREVIATIONS

AB – Acid-base

CCUS – Carbon capture, utilization and storage

CF – Carbon footprint

CO – Clay oxalate

COC – Clay oxalate cement

C$\overline{S}$A – Calcium sulfoaluminate

C$\overline{S}$ACO – C$\overline{S}$A clay oxalate

DBM – Dead-burned magnesia

GHG – Greenhouse gases

HYBCO – Hybrid clay oxalate

LOI – Loss on ignition

MCO – Magnesium clay oxalate

MIP – Mercury intrusion porosimetry

OA – Oxalic acid

PC – Portland cement

SEM – Scanning electron microscopy

TGA – Thermogravimetric analysis

wt. % – Percent by weight

XRF – X-ray fluorescence

XRD – X-ray diffraction

CHAPTER 1

INTRODUCTION

1.1 Research Background

The world is facing the threat of global warming and climate change due to the rapid increase in population, industrialization, and intensive waste generation. In 2015, many countries, including major polluters like China, the United States, and the European Union, signed the Paris Agreement at the United Nations Climate Change Conference to challenge the adverse effects of climate change, such as severe natural disasters caused by extreme weather conditions and loss of biodiversity and human health. The stakeholders agreed to shift towards net-zero emissions, bringing down greenhouse gas (GHG) emissions as close to zero as possible.

Concrete is by far the most used building material and the second most used material by humans after water (Gagg, 2014; Monteiro et al., 2017). It is inexpensive, easily reached worldwide, and has outstanding engineering properties. It is made by mixing cement (usually Portland cement or its blends), aggregates, and water. High demand for concrete leads to the production of cement in large quantities. The world's total cement production hit 4.17 billion tonnes in 2020, continuing its increase (CEMBUREAU, 2022). However, cement production has an immense impact on ecology. Its raw materials (limestone and clay) are calcined at around 1450 °C to produce cement, which is an energy-intensive process requiring fuel burning. Furthermore, CO_2 is released due to the thermal decomposition of limestone. The overall carbon footprint of cement production varies from 0.8 to 1.2 tonnes per tonne of Portland cement (PC) (Aitcin, 2008). The cement industry is responsible for 3.8 % of the total GHG emissions and 5 % of the total CO_2 emissions (Baumert et al., 2005). Monteiro et al. (2017) state that the emissions are even higher, as they deem the cement industry responsible for 8-9 % of the global anthropogenic CO_2.

Scientists and engineers have been searching for environmentally-friendly binders in response to the need to reduce the negative impacts of cement production. Acid-base (AB) cements are one of many alternative binders. Even though AB cements were initially developed in the dentistry domain, they have also been a research subject as a construction material, mainly owing to their higher early strength and more rapid setting compared to PC.

Given the adverse environmental impacts of PC production and the beneficial features of AB cements, this thesis will focus on the development of novel magnesium oxalate cement, which can be classified as a branch of AB cements. Oxalic acid (OA) was utilized in this study because, today, it can even be produced via the electrochemical processing of atmospheric CO_2. Hence, it has the potential to reduce the carbon footprint of cementitious building materials and help the world achieve the net-zero emissions goal. Moreover, magnesium oxide, or magnesia, was dead-burned and used. Later, to reduce the environmental impact of oxalate cement mixtures, dead-burned magnesia was substituted with another alternative binder, calcium sulfoaluminate ($C\overline{S}A$) clinker, because dead-burning magnesia consumes more energy and emits more CO_2 than $C\overline{S}A$ production. So, it is ecologically advantageous to reduce the magnesia content.

1.2 Objectives and Scope

The main research objectives of this study are to:

- Develop a proper method and a set of rules for clay oxalate cement production,
- Investigate the mechanical performance, microstructure, and water resistance of clay oxalate cement,
- Produce $C\overline{S}A$ clinker and investigate the effect of substituting $C\overline{S}A$ clinker for dead-burned magnesium oxide on mechanical, water stability, and microstructural properties of clay oxalate cement.

This thesis comprises five chapters. Chapter 1 provides the background for this research and the objectives set to be achieved. Chapter 2 reviews the information available in the literature related to AB cements, oxalic acid, recently emerging oxalate cements, magnesia, and C$\overline{S}$A cement. Chapter 3 explains the materials used, the methods employed, and the experiments performed in this study. Chapter 4 presents and discusses the results of the experiments explained in Chapter 3. Chapter 5 covers the conclusions and final remarks of the study and draws a route to further research.

CHAPTER 2

LITERATURE REVIEW

2.1 Introduction

This chapter presents background information and reviews the literature on acid-base cements, oxalic acid and the sustainable ways to produce it, magnesia and some magnesia-based cements, and calcium sulfoaluminate cement.

2.2 Acid-Base Cements

2.2.1 General Information

Acid-base (AB) cements have been known since the mid-1800s and have found distinct fields of application, from biomedical to construction, thanks to their admirable properties like faster setting, better adhesion, and higher early strength than those of gypsum and Portland cement (PC). After French civil engineer and chemist Stanislas Sorel's invention of the zinc oxychloride cement in 1855, which was the first AB cement reported, AB cements have been developed mainly in the domain of dentistry (Wilson & Nicholson, 1993).

Wilson & Nicholson (1993) and Prosser & Wilson (1986) mention that AB cements have been utilized in various ways. In the biomedical industry, AB cement is employed in dental fillings, biocompatible bone cement, and splint bandaging. On the other hand, in the construction industry, AB cements might be encountered in applications like repairing concrete, surfacing walls and floors, and producing underwater pipelines.

2.2.2 Reaction Mechanism

As the name implies, AB cements are formed by the reaction between acid and base, forming a load-bearing product. The acid (anion source), which is usually present as an aqueous solution of an organic or inorganic acid, donates protons to the solution. The base (cation source), generally metal oxides or silicates in powder form, dissolves in the solution and releases cations. Through hydrolysis, the reactions between cations and H_2O molecules create aquosols. Positively-charged aquosols react with anions in the solution to form salts. The interconnection of salt molecules in the solution leads to gel formation. Gel saturates and forms a connected network of crystalline, semicrystalline, or disordered solids (Wilson & Nicholson, 1993; Wagh & Jeong, 2003; Wagh, 2016). This process is depicted in Figure 2.1.

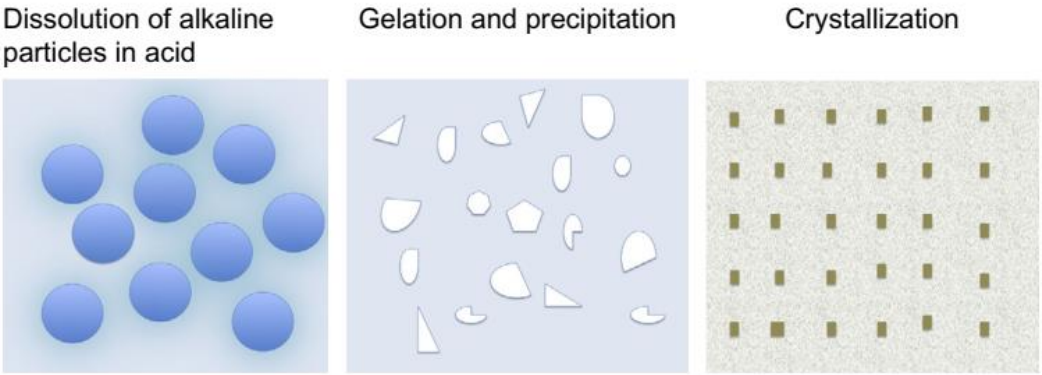

Figure 2.1 The stages of the formation of an acid-base cement (Wagh, 2016).

It is essential to control the dissolution rate of the base to form a well-ordered matrix. Crystallization of the gel, which results from the reaction between positively charged aquosols and anions from the acidic solution, is slow by nature. If the base dissolves too rapidly, the solution will saturate with the reaction products so rapidly that noncoherent precipitates will form. Otherwise, gel saturation will take a long time if the base dissolves too slowly. In such a case, the solution should remain still to grow a proper crystalline structure. Consequently, the base should not be exceedingly soluble or insoluble but sparsely soluble (Wagh, 2016).

2.3 Oxalic Acid and Oxalate Cements

2.3.1 General Information

Oxalic acid ($C_2H_2O_4$, OA in short) is the simplest dicarboxylic acid, which can be found in many natural plants, such as spinach and cocoa. It comes together with metals like Ca, Fe, Na, Mg, or K to form oxalates. Oxalates are also encountered in the human body, such as calcium or magnesium oxalates in kidney stones (Ivandini et al., 2006; Schuler et al., 2021).

OA has a wide range of consumer industries, from pharmaceutical to agriculture and textile. Other than the industries in which it is used as is, oxalic acid also has the potential to be the source of valuable chemicals, such as formic acid/formate and ethylene glycol, with market volumes of 900,000 and 30,000,000 tons per year, respectively (Schuler et al., 2021).

CO_2 promises to be a more prominent chemical source of OA production than realized today. There are multiple ways of producing OA today (Figure 2.2), some of which are commercially available while some are still in the development stage. The sustainable option might be via electrochemically processing carbon dioxide. On the other hand, after the Paris Agreement in 2015, more attention has been paid to carbon capture, utilization, and storage (CCUS) technologies in carbon-intensive industries like the cement industry, to decarbonize these industries to lower their global warming potential (Schuler et al., 2021; Kawai et al., 2022). OA production from CO_2 could be an excellent route to make use of the captured carbon by combining these two emerging environmentally-friendly methods.

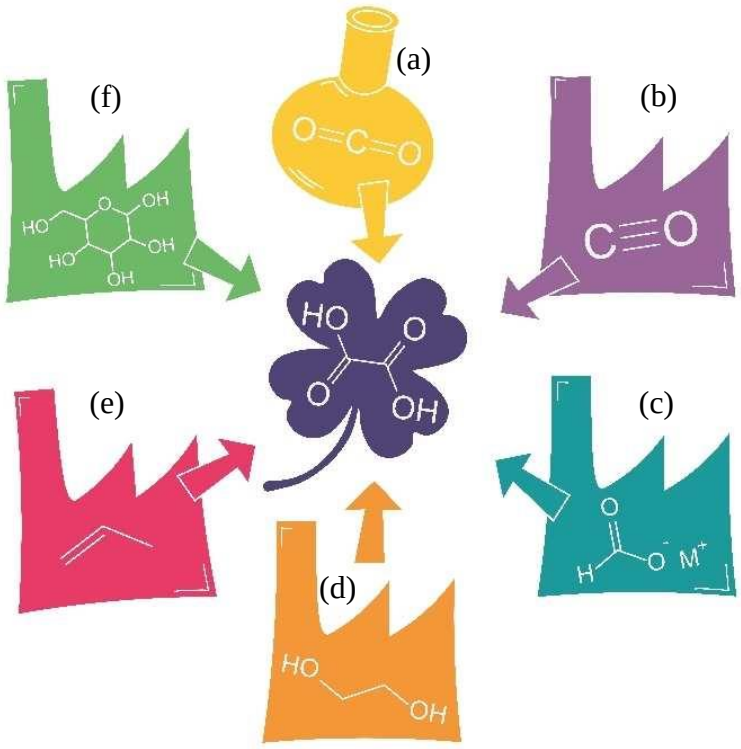

Figure 2.2 Six primary feedstocks by which oxalic acid is produced: (a) CO_2, (b) CO, (c) alkali formate, (d) ethylene glycol, (e) propylene, and (f) carbohydrates (Schuler et al., 2021).

Captured CO_2 can be directly converted to OA, although there is not a commercial way currently due to the low efficiency of systems. Schuler et al. (2021) defined three routes for the direct conversion of CO_2 into OA: direct electrochemistry, CO_2 reduction catalyzed homogeneously by metal complexes, and reduction of CO_2 with Ca-ascorbate and electrochemical regeneration. Schuler et al. (2021) summarize the production of OA via direct electrochemical CO_2 reduction as follows:

CO_2 is reduced to CO_2^- by a single electron. The resulting anion is very reactive; thus, it forms formate and carbonate instead of oxalate in the presence of water, as shown in Equation 2.1.

$$2CO_2 + 2e^- \rightarrow 2CO_2^-$$
$$2CO_2^- + H_2O \rightarrow HCO_2^- + HCO_3^- \quad (2.1)$$

Therefore, water should be absent in the reaction medium. If CO_2^- stays sufficiently long on the electrode surface, it reacts with another one to form oxalate (Equation 2.2). Contrarily, if CO_2^- is not on the surface long enough, it moves into the electrolyte to react with another one, forming CO and CO_3^{2-} (Equation 2.3), not oxalate.

$$2CO_2 + 2e^- \rightarrow 2CO_2^- \rightarrow C_2O_4^{2-} \quad (2.2)$$

$$2CO_2 + 2e^- \rightarrow 2CO_2^- \rightarrow CO + CO_3^{2-} \quad (2.3)$$

The commercial zinc oxalate process uses a sacrificial zinc anode. The formation of insoluble zinc oxalate occurs here and is then filtrated from the electrolyte. CO_2 is reduced to oxalate (Equation 2.2), and zinc (Zn) is oxidized to Zn^{2+} (Equation 2.4) simultaneously. Oxalate anion and Zn^{2+} cation combine to form zinc oxalate (ZnC_2O_4). Zinc oxalate, then, is filtrated and mixed with sulfuric acid (Equation 2.5), forming oxalic acid and zinc sulfate. Electrolysis of zinc sulfate in water can recover zinc and sulfuric acid, as given in Equation 2.6.

$$Zn \rightarrow Zn^{2+} + 2e^- \quad (2.4)$$

$$ZnC_2O_4 + H_2SO_4 \rightarrow ZnSO_4 + H_2C_2O_4 \quad (2.5)$$

$$ZnSO_4 + H_2O \rightarrow Zn + H_2SO_4 + \frac{1}{2}O_2 \quad (2.6)$$

Finally, the summation of reactions in the zinc oxalate process yields Equation 2.7.

$$2CO_2 + H_2O \rightarrow H_2C_2O_4 + \frac{1}{2}O_2 \quad (2.7)$$

2.3.2 Oxalate Cements

Oxalate cements have emerged very recently as a subclass of AB cements. The idea is to use OA or its salts (anion source) with metal oxides (cation source) to form chemically bonded solids at ambient temperatures. The subject of oxalate cements

has not been studied well yet. Three studies were found regarding this topic in the literature. Among the three, two used magnesium as the alkaline precursor, making magnesium oxalate cement, while iron-rich copper slag was used in the other study to make ferrous oxalate cement.

2.3.2.1 Magnesium Oxalate Cement

Erdoğan et al. (2022) mixed dead-burned magnesia powder (calcined at 1500 °C, MgO1500) with oxalate salt. They reported that the pastes made with OA self-heated extremely and cracked upon setting due to vapor pressure. Therefore, OA was neutralized with NaOH or with a sulfate-rich high-lime Class C coal fly ash. The resulting OA salts were named as NaOx and FAOx, respectively. X-ray diffraction (XRD) results indicated that the principal minerals in NaOx and FAOx were sodium hydrogen oxalate monohydrate ($NaHC_2O_4 \cdot H_2O$) and whewellite ($CaC_2O_4 \cdot H_2O$), respectively. The hydration mechanism to form the main reaction product magnesium oxalate dihydrate ($MgC_2O_4 \cdot 2H_2O$, glushinskite) was explained by the reaction of Mg^{2+} with $HC_2O_4^-$ and $C_2O_4^{2-}$ dissolved from NaOx and FAOx, respectively. (Equations 2.8 and 2.9).

$$Mg^{2+} + HC_2O_4^- + 2H_2O \rightarrow MgC_2O_4 \cdot 2H_2O + H^+ \quad (2.8)$$

$$Mg^{2+} + C_2O_4^{2-} + 2H_2O \rightarrow MgC_2O_4 \cdot 2H_2O \quad (2.9)$$

The pH of magnesium oxalate (MgOx) pastes made with OA-as-is was measured as ~4 beyond 1 day, while the pH of MgOx pastes with NaOx (MgNaOx) and FAOx (MgFAOx) are both ~10. MgNaOx mortars with a water-to-powder (W/P) ratio of 0.35 and a sand-to-powder (S/P) ratio of 2 reached 10 MPa of compressive strength on day 3 and about 25 MPa on day 28. MgFAOx mortar using W/P=0.3 and S/P=2 resulted in a compressive strength above 30 MPa at 1d and nearly 45 MPa at 28d (Figure 2.3a). They also tested the water resistance of these mortars. After being

submerged in water for 28 days, MgNaOx mortar lost almost two-thirds of its ultimate strength, whereas MgFAOx lost only 5 % of its ultimate strength.

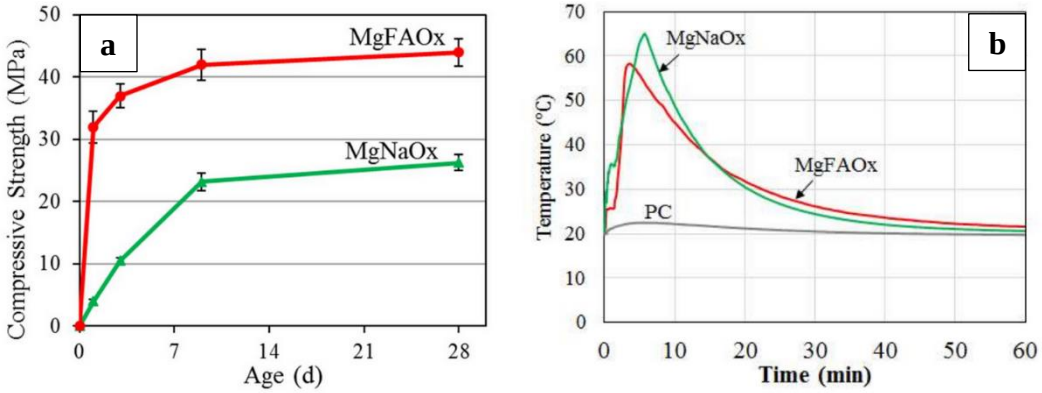

Figure 2.3 (a) Strength development of MgOx mortars, and (b) temperature evolution of MgOx pastes and PC. (Erdoğan et al., 2022).

According to mercury intrusion porosimetry results, MgFAOx paste had a smaller average pore size and porosity than MgNaOx. Thermal analyses showed that glushinskite decomposes with 24.3 % mass loss at 160-240 °C and 48.5 % at 400-500 °C. Calcium oxalate monohydrate decomposed in three steps: dehydrated at 150-200 °C, lost carbon monoxide and carbon dioxide at 450-500 °C, and 650-850 °C, respectively. The maximum temperature achieved during the magnesium oxalate reaction was dramatically higher than PC (Figure 2.3b). They also analyzed magnesium oxalate cement in terms of sustainability. As a result, it was concluded that MgFAOx has the potential to be carbon-neutral if a FAOx/MgO1500 ratio of 3.1 or greater is employed, pointing out the dependency of this ratio on FA/OA and oxide composition of the fly ash used. The estimated cost per m^3 of MgFAOx cement concrete was reported as 105-200 $, higher than that of PC concrete.

İçinsel (2020) prepared magnesium oxalate cement by neutralizing OA with hydrated (HCP) and dehydrated (DCP) cement mortars. The resulting salts of OA, named as HCPOx and DCPOx, were then mixed with quartz sand and dead-burned magnesia (1500 °C) to obtain magnesium oxalate mortars. XRD patterns of HCPOx and DCPOx mainly suggested the presence of whewellite and quartz (from sand in

crushed mortars) alongside some unreacted OA. Compressive strengths were determined for varying binder proportions at several ages. Magnesium oxalate mortars made with HCPOx outperformed the DCPOx mortars because the latter suffered from workability issues at the same water content as the former. At 28d, magnesium oxalate mortars of HCPOx reached ~16 MPa, while those of DCPOx had ~10 MPa. He also investigated the effect of boric acid as a retarder. Although setting times did not notably increase, the ultimate strengths of mortars dropped significantly, almost to half of the HCPOx-containing mortar. Furthermore, the effect of substituting silica fume or a Class F fly ash for a certain amount of sand was investigated. As a result, adding pozzolans required higher water content, thus leading to a decrease in strength. In the thermal analyses of magnesium oxalate pastes with recycled cement pastes, the decomposition of magnesium oxalate hydrate and calcium oxalate hydrate was observed.

2.3.2.2 Ferrous Oxalate Cement

Luo et al. (2021) developed ferrous oxalate cement by combining iron-rich copper slag (CS) and OA. Dry powders of CS, OA, and borax ($Na_2B_4O_7 \cdot 10H_2O$, or B) were milled with different CS/OA and borax-to-cement ratios (B/C), then water was added to dry powder mix with various water-to-cement ratios (W/C). 20 mm × 20 mm × 20 mm paste specimens with the CS/OA ratio of 3.6 gave the highest strength, reaching ~53 MPa at 28d (Figure 2.4a). Setting time gets longer as OA content lowers (Figure 2.4a). The pH of FOC paste with CS/OA=3.6 was measured as ~4.5 three hours after the start of hydration.

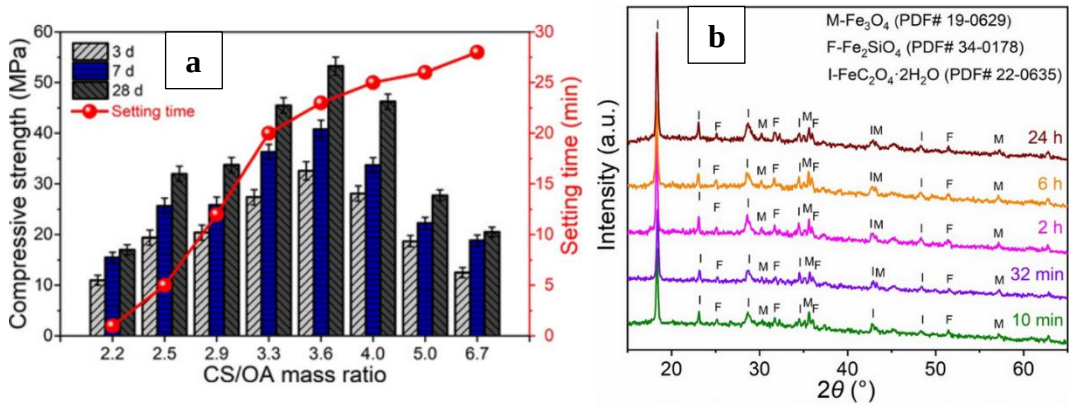

Figure 2.4 (a) Compressive strength and setting time of FOC paste specimens with changing CS/OA, and (b) XRD patterns of FOC paste with CS/OA = 3.6 (Luo et al., 2021).

As the B/C ratio increased from 0.00 to 0.04, the hardening of FOC mixtures was delayed up to 44 minutes. However, using a B/C ratio higher than 0.03 significantly decreased the strength. Higher B/C also led to lower heat evolution upon hydration and higher pH for FOC suspensions. As a result of the study, optimal paste proportions were proposed to achieve high strength and sufficiently long setting time as follows: CS/OA=3.6, B/C=0.03, W/C=0.18. Moreover, they investigated the FOC formation mechanism. Fe_3O_4 and Fe_2SiO_4 present in CS dissolved in the acidic solution, giving up Fe^{2+} cations, which reacted with $HC_2O_4^-$ and $C_2O_4^{2-}$ anions in the solution to form iron oxalate hydrate ($FeC_2O_4 \cdot 2H_2O$) as presented in Equations 2.10 and 2.11, respectively. Iron oxalate hydrate was the predominant mineral observed in XRD analyses of hydrated FOC (Figure 2.4b).

$$Fe^{2+} + HC_2O_4^- + 2H_2O \rightarrow FeC_2O_4 \cdot 2H_2O + H^+ \quad (2.10)$$

$$Fe^{2+} + C_2O_4^- + 2H_2O \rightarrow FeC_2O_4 \cdot 2H_2O \quad (2.11)$$

2.4 Magnesia

2.4.1 General Information

Magnesium is the eighth most abundant element in the Earth's crust (~2.3 % by weight) and the third most abundant element in seawater solution with ~1300 ppm or 1.3 g/L (Wagh, 2016; Nobre et al., 2020). Magnesium oxide (MgO or magnesia) is the most commonly encountered magnesium compound. Global magnesia production capacity by 2018 was 26.4 million tons per year. Turkey's annual magnesia production capacity is 975,000 tons, the third highest in the world after China (16.9 million tons) and Russia (2.88 million tons) (USGS, 2022).

Today, magnesia is produced in two main ways, and both these methods are energy intensive. The first way, which accounts for the more significant proportion of total production, is by calcining magnesium carbonate ($MgCO_3$ or magnesite) until it releases its CO_2. The second is by calcining magnesium hydroxide ($Mg(OH)_2$ or brucite) precipitated from seawater or magnesium-bearing brines through either a series of chemical processes or carbonation methods (Walling & Provis, 2016; Nobre et al., 2020; Shand et al., 2020).

The first magnesia production method (dry method), which involves heating magnesite to above 600 °C after crushing it (Walling & Provis, 2016), is formulated in Equation 2.12. It is similar to the production of lime by calcining limestone. Assuming molar masses of MgO and CO_2 as 40 and 44 g/mol, respectively, 1.08 tons of CO_2 is released to obtain 1 ton of MgO by calcining pure magnesite. From an environmental point of view, this value is higher than CO_2 emitted per tonne of cement, which is 0.8-0.9 tonnes on the global average (Jahren & Sui, 2013).

$$MgCO_3 + \text{Heat} \xrightarrow{>600\ ^\circ C} MgO + CO_2 \qquad (2.12)$$

Besides, the amount of CO_2 emitted from magnesia production is also related to the kiln temperature. Determined by the desired reactivity of MgO, there are four main types of magnesia produced by adjusting kiln temperatures. Light-burned (caustic-calcined) magnesia, calcined at 700-1000 °C, has the highest specific surface area and reactivity. Light-burned magnesia is utilized in various industries, such as agriculture, paper, and pharmaceutical. Hard-burned magnesia, calcined at 1000-1500 °C, has a lower specific surface area and reactivity than light-burned magnesia. Dead-burned magnesia, calcined at 1500-2000 °C, is even lower in surface area and reactivity. Dead-burned magnesia, which will be encountered in this thesis, is used in the refractory and cement industries. Fused magnesia, calcined at temperatures above 2800 °C, has the lowest reactivity. The energy required and CO_2 emitted increases with kiln temperature, as expected (Walling & Provis, 2016; Nobre et al., 2020).

The second method for producing magnesia (wet method) is the precipitation of $Mg(OH)_2$ from a solution rich in magnesium through complex chemical processes. The wet method yields the production of purer magnesia than the dry method, but the energy requirement of the wet method is three times higher than that of the dry method. In the wet method, Mg-rich solution (seawater or brine) is pre-treated with sulfuric acid (H_2SO_4) to remove carbonates (Equation 2.13) and obtain a solution rich in $MgCl_2$. Then, the solution rich in $MgCl_2$ is reacted with slaked lime ($Ca(OH)_2$) or dolime ($CaMg(OH)_4$) to precipitate $Mg(OH)_2$ as illustrated in Equations 2.14 and 2.15, respectively. After the precipitated $Mg(OH)_2$ slurry is filtered and washed, it is calcined at 350 °C (Walling & Provis, 2016; Devasahayam & Strezov, 2018; Nobre et al., 2020; Shand et al., 2020). Figure 2.5 illustrates the route for producing MgO through the wet process.

$$Ca(HCO_3)_2 + H_2SO_4 \rightarrow CaSO_4 + 2CO_2\uparrow + 2H_2O \quad (2.13)$$

$$MgCl_2 + Ca(OH)_2 \rightarrow Mg(OH)_2\downarrow + CaCl_2 \quad (2.14)$$

$$MgCl_2 + CaMg(OH)_4 \rightarrow 2Mg(OH)_2\downarrow + CaCl_2 \quad (2.15)$$

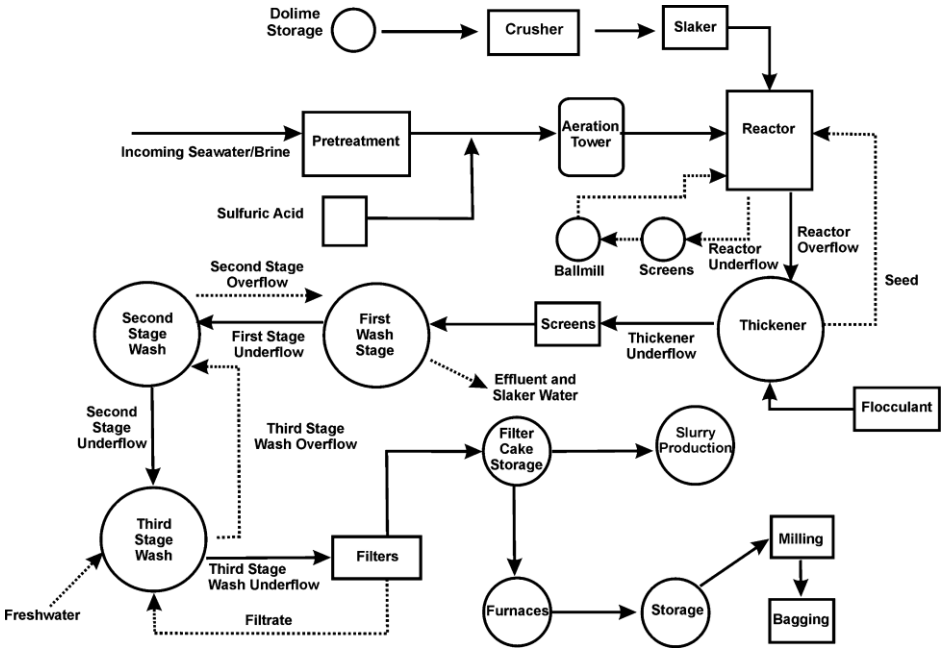

Figure 2.5 Flow diagram of the wet method (Shand et al., 2020).

One other alternative for the wet method is the pyrohydrolysis of magnesium chlorides in 1000 ℃ steam (Equation 2.16).

$$MgCl_2 \cdot 6H_2O \xrightarrow{\sim 1000\ ^\circ C} MgO + 2HCl + 5H_2O \qquad (2.16)$$

2.4.2 Magnesium Phosphate Cement

Magnesium phosphate cement (MPC) is formed by mixing magnesia powder with acid phosphate in an aqueous environment (Odler, 2000). The acid phosphate may be ammonium dihydrogen phosphate ($NH_4H_2PO_4$), ammonium hydrogen phosphate ($(NH_4)_2HPO_4$), sodium tripolyphosphate ($Na_5P_3O_{10}$), potassium dihydrogen phosphate (KH_2PO_4), aluminum hydrogen phosphate, or magnesium dihydrogen phosphate ($Mg(H_2PO_4)_2$) (Shand et al., 2020). Among the given, ammonium dihydrogen phosphate and potassium dihydrogen phosphate are the most widely used. The system is called magnesium ammonium phosphate cement (MAPC) and magnesium potassium phosphate cement (MKPC) when the former and latter are

used as the acid source, respectively. MPCs have found various application fields, such as quick repair of roads and floors, radioactive and hazardous waste stabilization, and shielding against nuclear radiation (Wagh, 2016).

MgO is sparsely soluble in water, but its solubility becomes higher in a phosphoric acid solution. The acid-base reaction between MgO powder and phosphoric acid is fierce even when the acid solution is diluted, leading to noncoherent precipitates, as described in Section 2.2.2. Therefore, acid phosphate salts, which are higher in pH (less acidic) than phosphoric acid solution, are used to control the reaction rate when manufacturing MPC (Odler, 2000; Shand, 2006). The reaction rate can also be controlled by calcining MgO. Once MgO is burned at temperatures >1300 °C, the individual MgO particles become bigger and denser. As the calcination temperature and residence time increase, the specific surface area of the individual MgO grain decreases, making MgO less soluble and hence less reactive (Wagh & Jeong, 2003). Figure 2.6a presents the pH of the solution in which MgO and H_3PO_4 are mixed. It can be inferred that the calcination reduces the solubility of MgO.

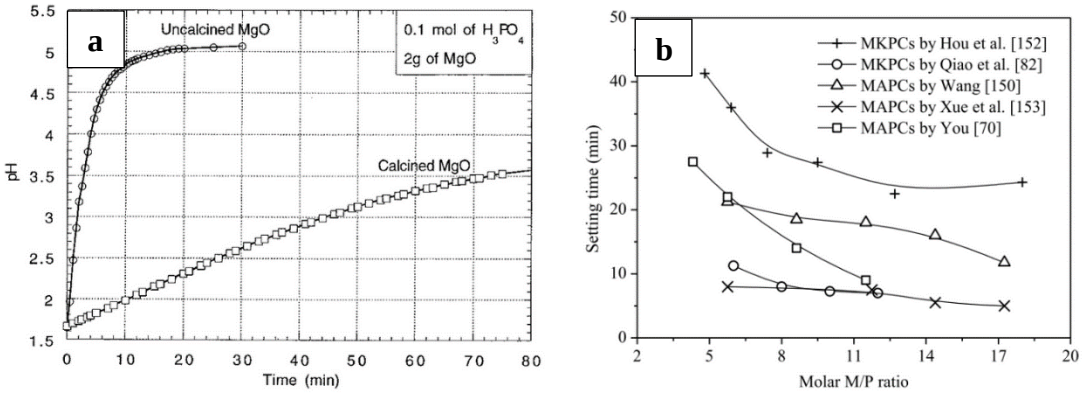

Figure 2.6 (a) The change in pH with time after adding MgO to an H_3PO_4 solution (Wagh & Jeong, 2003), and (b) the change in setting times of MPCs with M/P (Shand et al., 2020).

The setting time of MAPC is slightly shorter than that of MKPC due to the higher solubility of the acid phosphate used in MAPC. Figure 2.6b suggests that setting times tend to decrease with increasing magnesium-to-phosphate molar ratio (M/P).

Using less acidic phosphates can help produce MPC with longer setting times. For example, the setting time of MKPC made with KH_2PO_4 increased from 5 minutes to 180 minutes after replacing KH_2PO_4 with K_2HPO_4 (Shand et al., 2020).

Another way to control the reaction rate is to use boric acid or borates. Boron compounds cover the surface of MgO grains to retard the setting (Wagh, 2016). However, Tan et al. (2016) point out that using boric retarders results in increased costs. Gelli et al. (2022) demonstrated the effect of borax on the fluidity and setting time of MPC pastes. Higher borax content resulted in a higher flow of MPC paste (Figure 2.7a). As plotted in Figures 2.7b and 2.7c, adding 10 % borax by mass of tri-magnesium phosphate (TMP, the basic powder used in their study) led to delaying the final setting time of MPC paste up to over 80 minutes. Even though adding borax helps gain more time for workability, Yang & Qian (2010) found that using 7.5-10 % borax had a positive effect on the late strength, while the utilization of less than 7.5 % or more than 10 % of borax gave relatively lower strength (Figure 2.8).

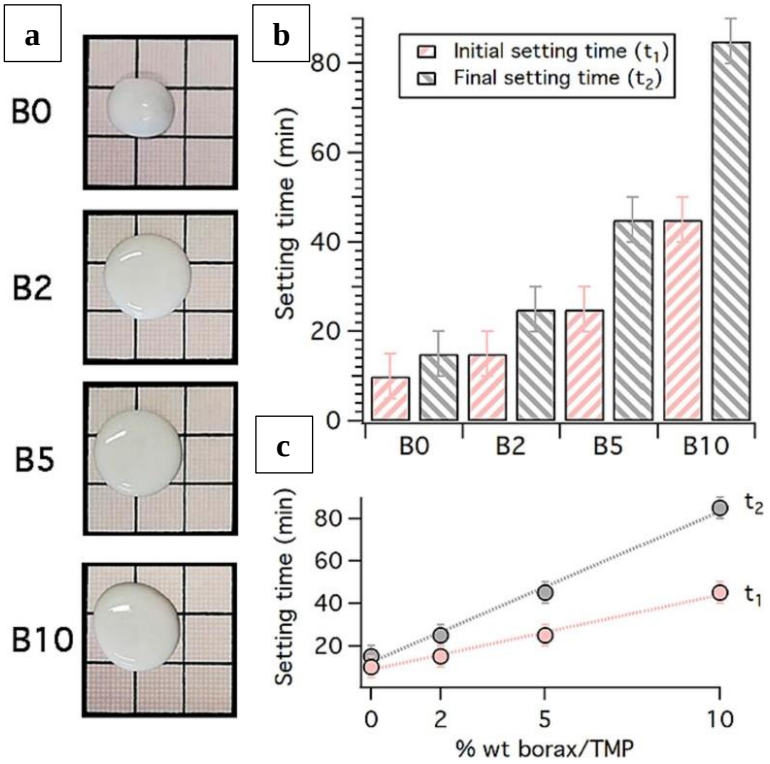

Figure 2.7 (a) Images of MPC pastes with increasing borax content from top to bottom, and (b-c) initial and final setting times of MPC pastes. (Gelli et al., 2022).

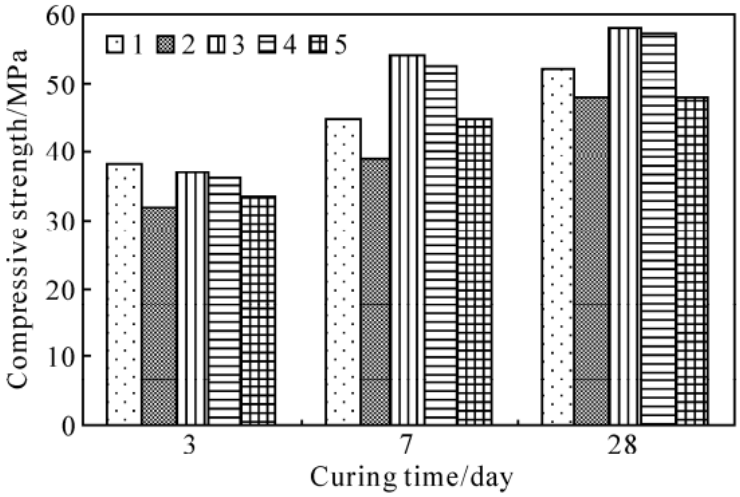

Figure 2.8 The effect of increasing the borax-to-magnesia ratio (from 2.5 % (mix 1) to 12.5 % (mix 5) by 2.5 % increments) on the strength of MKPC pastes. (Yang & Qian, 2010).

Hydration reactions of ammonium dihydrogen phosphate, diammonium hydrogen phosphate, and potassium dihydrogen phosphate with dead-burned magnesia are given in Equations 2.17, 2.18, and 2.19, respectively.

$$MgO + NH_4H_2PO_4 + 5H_2O \rightarrow NH_4MgPO_4 \cdot 6H_2O \quad (2.17)$$

$$MgO + (NH_4)_2HPO_4 + 5H_2O \rightarrow NH_4MgPO_4 \cdot 6H_2O + NH_3\uparrow \quad (2.18)$$

$$MgO + KH_2PO_4 + 5H_2O \rightarrow KMgPO_4 \cdot 6H_2O \quad (2.19)$$

In Figure 2.9, the pH of MAPC with changing M/P is compared to that of MKPC with M/P=1. pH increases with increasing M/P. The pH of MAPC mixtures made with ammonium dihydrogen phosphate was 5-6 for M/P=2 and M/P=3, while a pH of 9-10 was achieved for M/P≥5. On the other hand, the pH of the MKPC mixture prepared with potassium dihydrogen phosphate was ~7.5 though its M/P ratio was even smaller than that of MAPC mixtures. The pH development rate of the MKPC mixture was also lower than those of MAPC mixtures, which may be why MKPC is slower than MAPC in the setting.

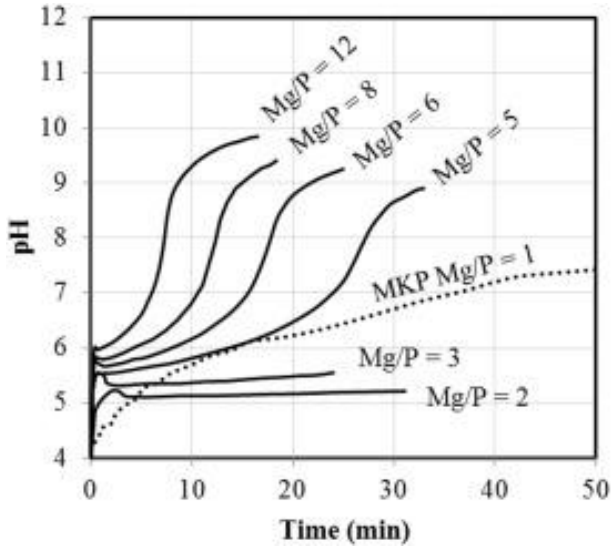

Figure 2.9 Comparison of the pH of MAPC (solid curves) and MKPC (dotted curve) (Le Rouzic et al., 2017).

2.5 Calcium Sulfoaluminate Cement

2.5.1 General Information

Calcium sulfoaluminate ($C\overline{S}A$) cement was designed and industrialized by the China Building Materials Academy in the 1970s (Yuan et al., 2021). The main compounds of its clinkers are ye'elimite ($C_4A_3\overline{S}$), belite (C_2S), ferrite phase (C_4AF), and anhydrite ($C\overline{S}$). In $C\overline{S}A$ clinker, ye'elimite content varies between 35 and 70 wt. %, while the belite and ferrite phases are present in considerable amounts, as well.

$C\overline{S}A$ cement is deemed a low-energy cement because of lower calcination temperatures of 1250-1350 °C compared to PC, about 1450 °C. As can be inferred from Table 2.1, its low energy requirement can be linked to the lower enthalpy of ye'elimite formation than alite (C_3S), the main compound of PC. Since the CO_2 emitted upon the formation of ye'elimite is less than half of alite's, $C\overline{S}A$ cement can also be regarded as eco-friendly.

Table 2.1 Energy requirement and CO_2 released during the formation of cement compounds. Adapted from Sharp et al. (1999).

Cement compound	Enthalpy of formation (kJ/kg-clinker)	CO_2 released (kg/kg-clinker)
C_3S	1848.1	0.578
β-C_2S	1336.8	0.511
$C_4A_3\overline{S}$	~800	0.216

C$\overline{S}$A clinkers can be produced by combining limestone, clay, bauxite, and gypsum/anhydrite (Yuan et al., 2021). During clinkering of C$\overline{S}$A systems, C_2AS forms first at 900 °C and reacts with C$\overline{S}$ at 1000 °C to form $C_4A_3\overline{S}$ and α'-C_2S, finally disappearing at 1200 °C. Contingent upon the A/F ratio, ferrite phases form with variable composition (Sharp et al., 1999).

2.5.2 Hydration Mechanism

Ettringite ($C_6A\overline{S}_3H_{32}$) is the main hydration product of C$\overline{S}$A cement. It contributes to the early strength development of C$\overline{S}$A cement. It is formed by the hydration of ye'elimite in the presence of anhydrite (Equation 2.20) or gypsum (Equation 2.21). In the absence of a sulfate source such as gypsum, ye'elimite hydrates to form monosulfate ($C_4A\overline{S}H_{12}$) as described in Equation 2.22. Monosulfate becomes ettringite when sufficient sulfate and water are available in the pore solution (Equation 2.23). The hydration of ye'elimite also yields amorphous AH_3 (Brien et al., 2013; Canbek et al., 2020; Odler, 2000; Yuan et al., 2021).

$$C_4A_3\overline{S} + 2C\overline{S} + 38H \rightarrow C_6A\overline{S}_3H_{32} + 2AH_3 \quad (2.20)$$

$$C_4A_3\overline{S} + 2C\overline{S}H_2 + 34H \rightarrow C_6A\overline{S}_3H_{32} + 2AH_3 \quad (2.21)$$

$$C_4A_3\overline{S} + 18H \rightarrow C_4A\overline{S}H_{12} + 2AH_3 \quad (2.22)$$

$$2C_4A\overline{S}H_{12} + 2C\overline{S} + 52H \rightarrow C_6A\overline{S}_3H_{32} + C_4A\overline{S}H_{12} + 4AH_3 \quad (2.23)$$

Belite in C$\bar{S}$A clinker hydrates to produce C-S-H and portlandite (Equation 2.24), as it does in PC (Yuan et al., 2021).

$$C_2S + (x+2-y)H \rightarrow C_ySH_x + (2-y)CH \qquad (2.24)$$

According to Fukuhara et al. (1981), C_4AF and gypsum react in an aqueous environment to form some amorphous ferrite hydrates and ettringite (Equation 2.25).

$$C_4AF + 3C\bar{S}H_2 + 35\frac{1}{3}H \rightarrow \frac{4}{3}C_3(A_{0.75},F_{0.25})\cdot 3C\bar{S}\cdot H_{31} + \frac{2}{3}FH_3 \qquad (2.25)$$

Sharp et al. (1999) presented XRD patterns for C$\bar{S}$A cement. Ferrite, ye'elimite, and belite phases were found in C$\bar{S}$A clinker. Ettringite was the main crystal observed after hydration, while the belite that was present at the early ages of hydration disappeared upon late activation. Canbek (2018) also investigated XRD patterns of a C$\bar{S}$A cement (~50 % ye'elimite, ~30 % brownmillerite, ~15 % belite, clinker-to-gypsum ratio of 81:19) at 1, 3, and 28 days of hydration (Figure 2.10). Unreacted ye'elimite, brownmillerite, and gypsum were observed together with ettringite even at 28d of hydration.

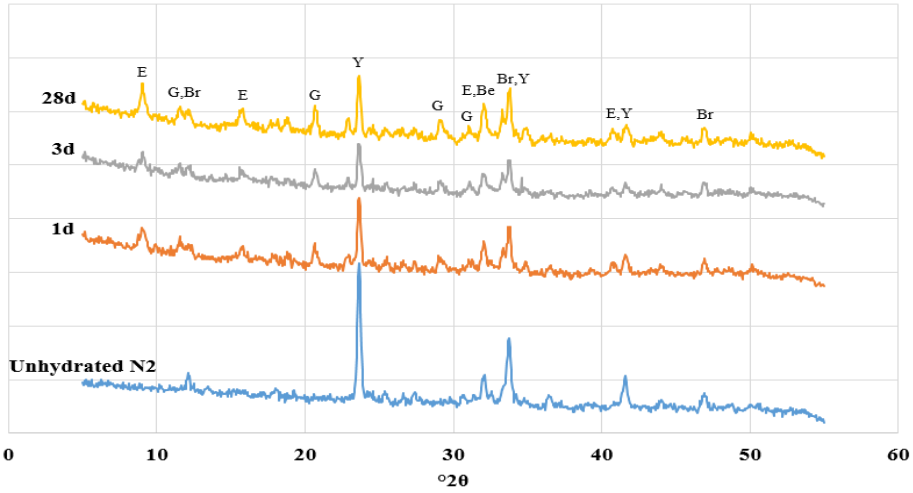

Figure 2.10 XRD patterns of C$\bar{S}$A clinker and hydrated C$\bar{S}$A cement at 1, 3, and 28 days of hydration (Canbek, 2018).

CHAPTER 3

EXPERIMENTAL PROCEDURE

The experimental procedure followed and the materials used in this study are introduced in this chapter.

3.1 Materials

3.1.1 Oxalic Acid

Technical-grade oxalic acid dihydrate ($C_2H_2O_4 \cdot 2H_2O$, OA in short) in powder form was used as the source of anions in acid-base mixtures. The pH of OA was measured as 1.00 at 0.00119 molality. OA was not used "as is" in mixtures and was partially neutralized with the addition of clay.

3.1.2 Clay

Clay procured from Votorantim Hasanoğlan Cement Plant in Ankara, Turkey was used to produce clay oxalate. To calculate its loss on ignition (LOI), after being preheated at 110 °C for 24 hours, the clay was calcined at 1050 °C for two hours. The oxide composition determined by X-ray fluorescence (XRF) spectrometry and the LOI of the clay are given in Table 3.1.

Table 3.1 The oxide composition and the LOI of the clay used.

Oxide	**Mass (%)**
SiO_2	56.20
Al_2O_3	19.10
Fe_2O_3	8.39

Table 3.1 continued.

CaO	7.16
MgO	2.51
K_2O	2.60
TiO_2	1.15
SO_3	1.08
LOI (%)	8

Nevertheless, the so-called clay used in this study might not be clay but only a silicon source utilized in cement production. Figure 3.1 shows that quartz is the main mineral in this clay. Also, the XRD analysis did not detect clay minerals like kaolinite or illite except for some montmorillonite peaks. On the other hand, some peaks could not be identified. Still, the material was treated as clay.

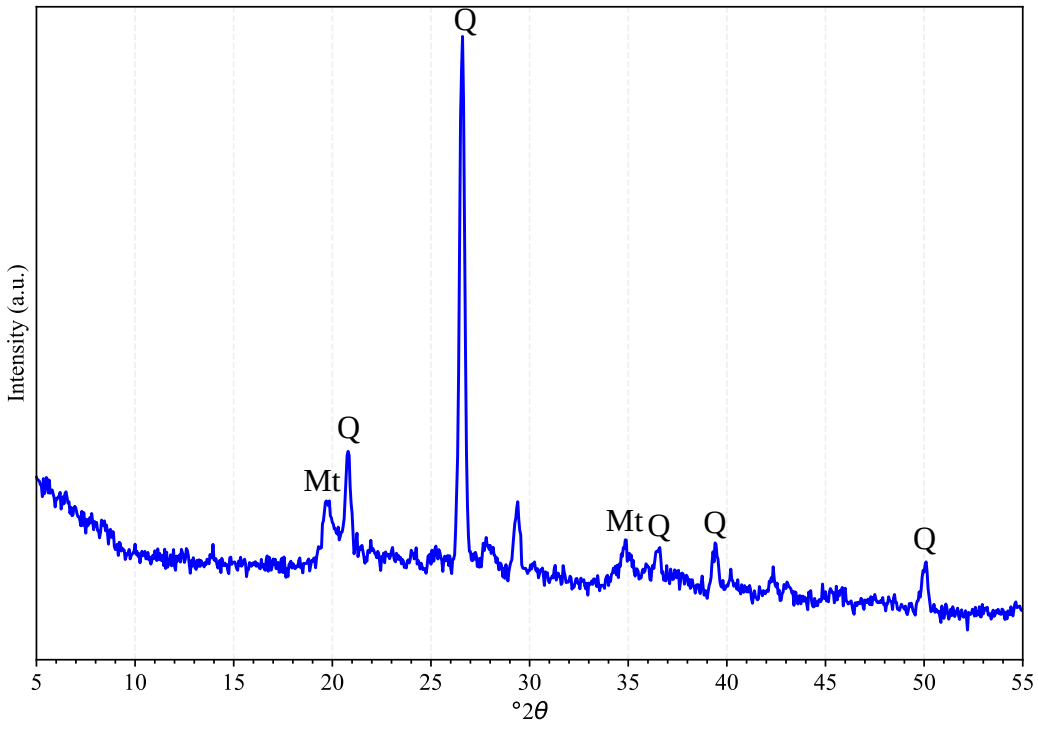

Figure 3.1 XRD pattern of the clay used. (Q: quartz, Mt: montmorillonite)

3.1.3 Dead-burned Magnesia

Magnesia (MgO) powder was dead-burned at 1500 °C for one hour inside alumina crucibles, as described by Bilginer (2018). Upon cooling after calcination, the powder inside the crucible turned into a hard mass. The hard mass was ground and sieved until 95 % of it passed through the 150-µm sieve to obtain dead-burned magnesia (DBM).

The effect of the calcination on the specific gravity of the ground and sieved magnesia was also analyzed by Bilginer (2018). As shown in Figure 3.2, the specific gravity increases with the calcination temperature. At 1500 °C, the specific gravity of magnesia is around 3.48.

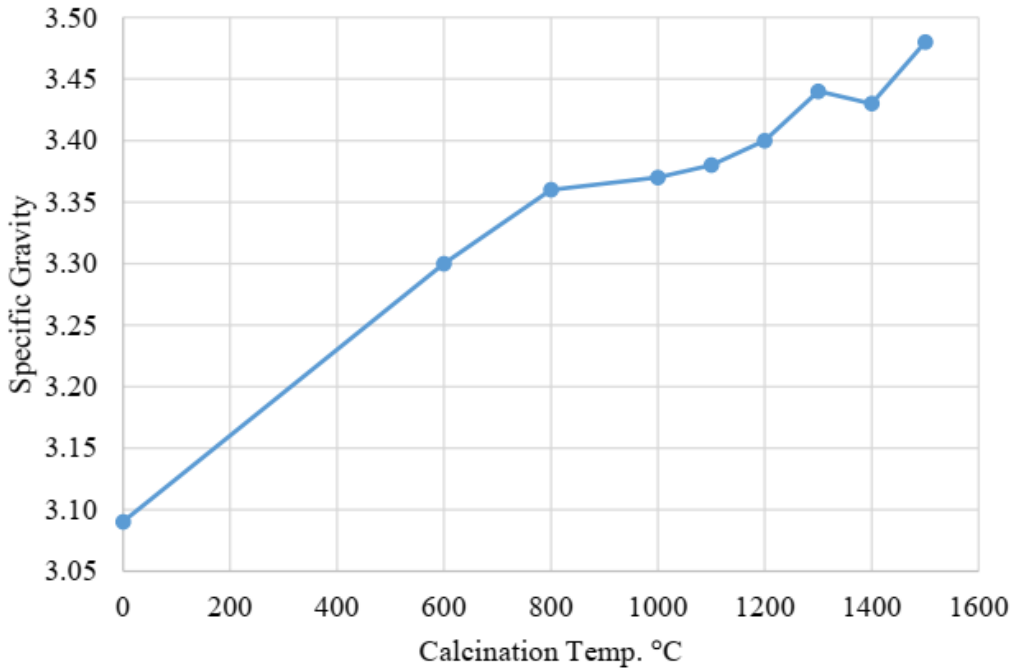

Figure 3.2 The effect of calcination on the specific gravity of magnesia (Bilginer, 2018).

3.1.4 Raw Materials Used in C$\bar{S}$A Clinker Production

Limestone, gypsum, and bauxite were used as raw materials while producing C$\bar{S}$A clinker. Limestone and gypsum were procured from Votorantim Hasanoğlan Cement Plant, while bauxite was supplied by Demireller Mining Inc. Raw materials were air-dried and ground in a ball mill until 95 % passed through the 150-μm sieve. The raw materials were calcined at 1050 °C with a residence time of two hours after preheating at 110 °C for 24 hours, as done for the clay, to find their LOI. Table 3.2 shows the oxide compositions of these raw materials.

Table 3.2 The oxide compositions of raw materials used in C$\bar{S}$A clinker production.

Oxide	**Limestone (%)**	**Gypsum (%)**	**Bauxite (%)**
SiO_2	2.96	4.55	13.40
Al_2O_3	1.44	1.64	50.00
Fe_2O_3	0.61	1.07	27.90
CaO	49.86	34.86	2.15
MgO	0.73	0.33	0.45
K_2O	0.17	0.26	1.27
TiO_2	0.00	0.13	3.41
SO_3	0.16	42.18	0.07
LOI (%)	42	15	15

In Figure 3.3, the XRD pattern of the C$\bar{S}$A clinker produced is shown. The main compound in the C$\bar{S}$A clinker was ye'elimite (peaks at ~24, ~34, and ~42 °2θ). Brownmillerite (peaks at ~12, ~32, ~34, and ~47 °2θ) and belite (peak at ~32 °2θ) were other compounds found in the clinker.

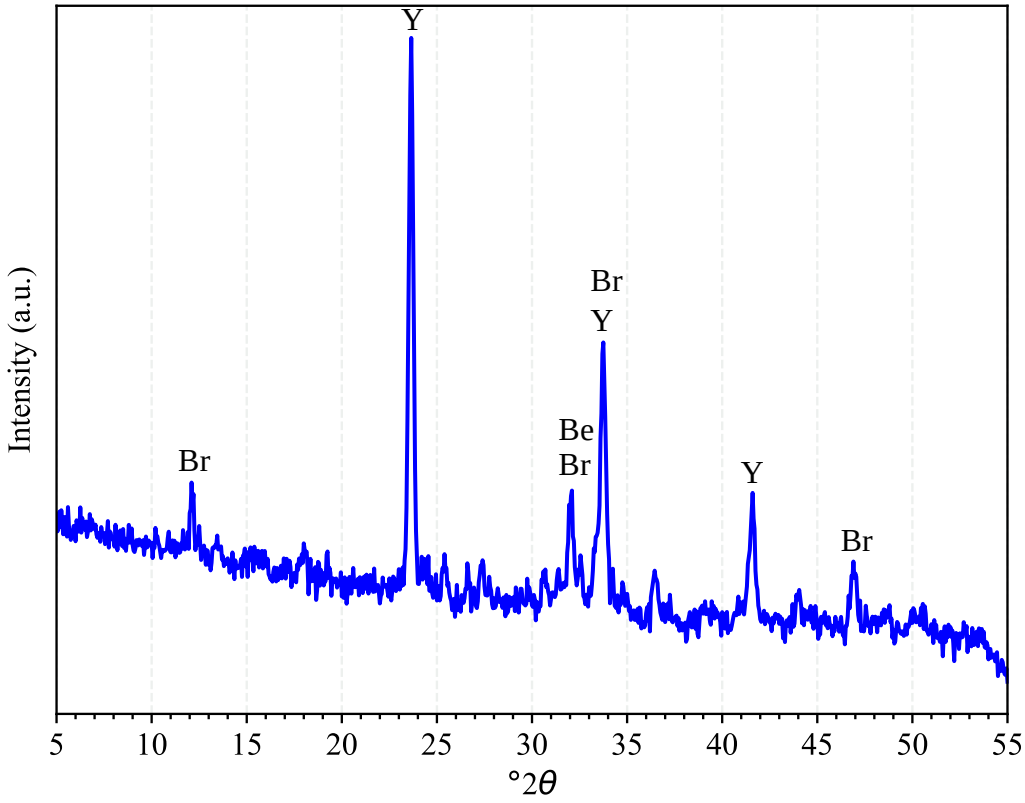

Figure 3.3 XRD pattern of C$\bar{S}$A clinker prepared. (Br: brownmillerite, Y: ye'elimite, Be: belite)

3.2 Methods

3.2.1 Production of Clay Oxalate

Experiences from preliminary laboratory research showed that mixtures made with OA-as-is reached remarkably high reaction rates; hence a noncoherent precipitate forms upon mixing with metal oxides. Nevertheless, it is known that if the reaction rate between acid and base is controlled, the development of coherent bonds between reacting particles can be developed (Wagh, 2016).

Clay was selected in this study to partially neutralize oxalic acid and slow down the acid-base reaction. The final product is called "clay oxalate" (CO). The main reason

clay was selected for the neutralization and replacement of OA is that it is abundant and inexpensive.

Small preliminary batches of CO batches were prepared preliminarily to determine an optimal ratio. Three different clay-to-oxalic-acid ratios (C/OA), 0.67, 1.00, and 1.50, by mass, were selected for paste trials (Table 3.3).

Table 3.3 C/OA used in the preliminary works to produce CO.

ID	C	OA
CO-0.67	1	1.5
CO-1.00	1	1
CO-1.50	1.5	1

While preparing magnesium clay oxalate (MCO) cement pastes, reaction rates of mixtures decreased with decreasing OA content, as one can expect. Observations also proved the difficulty of making MCO pastes when CO-0.67 is used due to its fast setting (high reactivity). Moreover, pastes made using CO-1.50 were cooler than those made with CO-0.67 and CO-1.00, so it was presumed that its clay content was more than required and hence not reactive enough. As a result of this preliminary work, CO-1.00 was selected for the remainder of the study. From this point on, CO refers to the clay-to-oxalic-acid ratio of 1.00.

CO is produced in four main stages: material mixing, oven drying, grinding, and sieving. A sample production guide for CO-1.00 is as follows:

1) 6 kg of OA is combined with 6 kg of deionized water and mixed for 5 minutes. Then, 6 kg clay is added gradually, and the mixing is continued for another 15 minutes until the frothing stops.
2) After the material mixing stage, the mixture is cast into shallow containers (Figure 3.4a) and allowed to dry at 105 ± 5 °C for three days to ensure complete water evaporation (Figure 3.4b).

3) CO is put into a laboratory ball mill and ground for around 20 minutes following the drying stage.
4) Ground CO is sieved through ASTM No. 100 sieve.

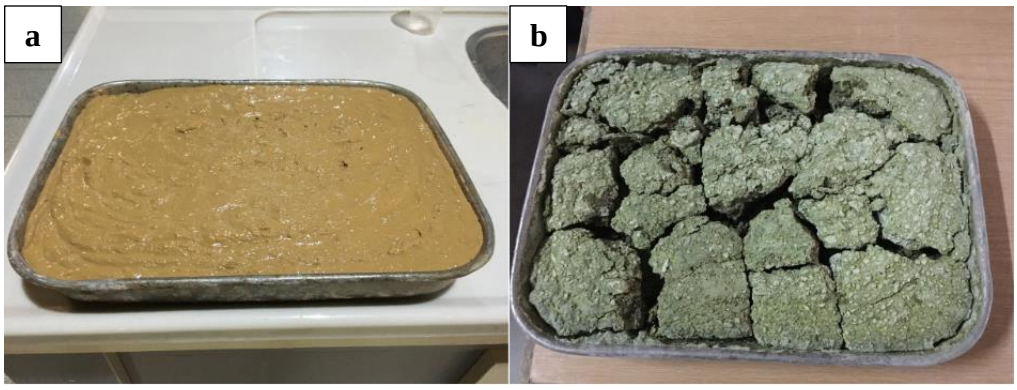

Figure 3.4 (a) CO after mixing and (b) CO after oven drying. The container in the pictures is 30 cm in length, 25 cm in width, and 5 cm in depth.

3.2.2 Production of C$\bar{S}$A Clinker

C$\bar{S}$A clinker was produced in the laboratory by combining raw materials and calcining them in a muffle furnace. Raw materials in powder form were initially dry-mixed in a mixing bowl until a homogeneous display was obtained, and deionized water was added with a water-to-powder ratio (W/P) of 0.25. Then, the mixture was mixed into a plastic clinker paste (like play dough) with a benchtop mixer following the procedure described in ASTM C305 (2020). The obtained paste was rolled into slender sticks approximately 1 cm in diameter and placed on refractory plates in a grid pattern (Figure 3.5) to ensure even calcination of clinker paste. The paste was heated up to 1300 ℃ at a rate of 10 ℃/min and resided for 2 hours at 1300 ℃ in a PROTHERM MoS-B 160/8 laboratory kiln.

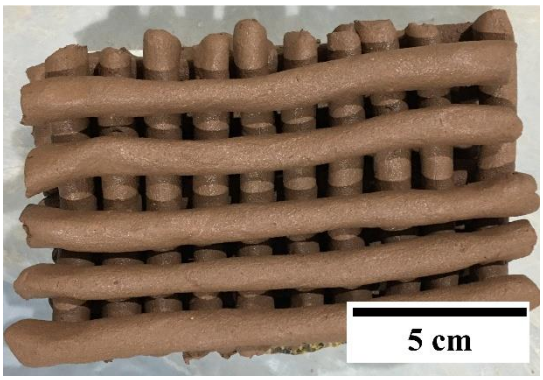

Figure 3.5 C$\bar{S}$A clinker paste shaped as slender sticks and ordered in a grid pattern.

The raw material proportion for C$\bar{S}$A clinker production is the same as the reference clinker (N2) defined in Canbek (2018): 40 % limestone, 40 % bauxite, and 20 % gypsum. LOI of a material is taken into account in calculating the amount of that material used in the clinker mixture—a sample calculation of a 1-kg batch of C$\bar{S}$A clinker is presented in Table 3.4.

Table 3.4 Sample calculation of raw materials proportion to produce 1 kg of C$\bar{S}$A clinker.

	Limestone	**Bauxite**	**Gypsum**	**Total**
Weight after calcination (g)	400	400	200	1000
LOI (%)	42	15	15	-
Weight before calcination (g)	$\frac{400}{1\text{-}0.42} = 690$	$\frac{400}{1\text{-}0.15} = 470$	$\frac{200}{1\text{-}0.15} = 235$	1395

3.2.3 Preparation of Clay Oxalate Cement with DBM and C$\bar{S}$A

A mixing method was developed after several trials for making magnesium clay oxalate (MCO), C$\bar{S}$A clay oxalate (C$\bar{S}$ACO), and hybrid clay oxalate (HYBCO) mixtures. HYBCO is made by combining DBM and C$\bar{S}$A clinker in equal parts.

MCO, C$\overline{S}$ACO, and HYBCO cements can all be referred to as “clay oxalate cement” (COC).

A benchtop laboratory cement mixer could not be employed in this study since setting times were too short for mixing and subsequent cleaning. Therefore, mixtures were prepared by hand mixing using a metal spoon.

1) CO is put into the mixing bowl.
2) Around 85 % of the total water is added and mixed with CO. The paste is sticky and likely to flocculate; hence, detected flocculations are squashed to avoid a drop in consistency later in the mixture.
3) Sand is mixed with the paste in halves. Since the paste is dense, adding all sand at once makes mixing harder at this step. If a paste is being prepared, this step is skipped.
4) After the remaining water is added, the DBM, C$\overline{S}$A, or an even blend of both is supplemented. The mixing is finalized when a homogeneous-looking paste or mortar is ensured. As the mixture tends to set quickly, this stage should not take more than 30 seconds.

Silica sand that conforms to EN 196-1 (2016) was used. Sand-to-binder ratio (S/B) used to prepare mortars was determined based on how the change in the ratio affected workability and mechanical properties. Mortar specimens with S/B of 2.50, 2.75, and 3.00 were visually inspected and tested at 1d for compressive strength. S/B=2.50 was employed instead of 2.75 in ASTM C109 (2020) because the workability of the mixture was already low due to CO’s being sticky and visibly reduced with increasing S/B. Furthermore, since this is a new type of cement and no plasticizer is known to work in this system, no admixture was utilized in this study despite the issues with workability.

3.2.4 Calculation of Carbon-Neutral COC Mix Proportions

Carbon footprint (CF) analyses were made for three separate pastes; MCO, HYBCO, and C$\overline{S}$ACO pastes. Optimal mix proportions for carbon neutrality of each type of oxalate cement were calculated. The overall logic is to use more OA to enable CCUS and less DBM to lower carbon emissions. Using more OA and less DBM than calculated makes the mixture carbon-negative, yet, increasing OA dosage makes the mix costlier, as mentioned in Section 2.3.2.1. Moreover, the CO_2 equivalent of energy requirement for producing CO, involving processes such as OA production, mixing, heating, and grinding, was neglected. It should be noted that producing OA via the direct conversion of CO_2 may be so energy-intensive that it can be carbon-positive unless renewable energy sources are employed. The reader is encouraged to repeat the calculations with distinct approaches and emission values.

3.3 Experiments

3.3.1 Compressive Strength

Compressive strength is one of the most prominent features to evaluate the performance of a cementitious system. Table 3.5 shows the CO/DBM/C$\overline{S}$A mass ratios used to investigate the compressive strength development of COC mortars. These ratios were selected such that the effect of CO dosage and replacing DBM with C$\overline{S}$A on the mechanical properties of COC mortars could be seen.

For example, to cast two cube mortar specimens of the mixture CO7-DBM, with a W/B of 0.35 and S/B of 2.50, the following amounts were used as ingredients:

- 140 g of CO
- 60 g of DBM
- 500 g of sand
- 70 g of deionized water

Table 3.5 Mixture proportions used in compressive strength tests.

ID	CO	DBM	$C\bar{S}A$
CO3-DBM	3	7	0
CO4-DBM	4	6	0
CO5-DBM	5	5	0
CO6-DBM	6	4	0
CO6-HYB	6	2	2
CO6-$C\bar{S}A$	6	0	4
CO7-DBM	7	3	0
CO7-HYB	7	1.5	1.5
CO7-$C\bar{S}A$	7	0	3
CO8-DBM	8	2	0
CO8-HYB	8	1	1
CO8-$C\bar{S}A$	8	0	2

Mortars were cast into 5-cm cube plexiglass molds in two layers and hand-tamped and shaken. Metal molds were not used since COC paste tends to stick to metal surfaces and disturb the smoothness of the sample surface. The cube specimens were demolded two hours after casting, which is possible due to COC's fast setting and high early strength. The samples were air-cured at ambient temperature and tested in compression at 6 hours, 1 day, 7 days, and 28 days with a Universal Testing Machine at a loading rate of 1.5 kN/s. Two cube specimens were used to determine compressive strength at the specified ages.

3.3.2 X-ray Diffraction Analysis

X-ray diffraction (XRD) is an analytical technique commonly used for characterizing cement (Scrivener et al., 2016). In this study, a series of qualitative XRD analyses were carried out for phase identification. A benchtop Olympus BTX-II device was used for scanning XRD powder samples between 5 and 55 °2θ with a resolution of

0.05 °2θ via CuKα radiation. The analyses of powder diffraction data were done using Crystallography Open Database (Gražulis et al., 2009, 2012).

CO-0.67, CO-1.00, and CO-1.50 powders were scanned and analyzed. Additionally, CO3-DBM, CO5-DBM, CO7-DBM, CO7-HYB, and CO7-C$\overline{S}$A pastes were used in XRD analyses, all with a W/B of 0.30. The pastes were selected so that the effect of CO dosage and replacing DBM with C$\overline{S}$A clinker on the mineral structures could be observed. Paste samples were kept under room conditions and inside separate containers, which were sealed via plastic foil to prevent the carbonation of samples. All samples were ground and passed through ASTM No. 100 sieve.

3.3.3 pH Measurement

CO7-DBM, CO7-HYB, and CO7-C$\overline{S}$A pastes were prepared using a W/B of 0.30. Paste samples were cured as described in Section 3.3.2. The pH of paste samples was tested at 1h, 3h, 6h, 1d, 7d, and 28d. At testing ages, hardened paste samples were ground using a mortar and pestle into powder and sieved through ASTM No. 100 sieve. 10 g of COC paste in powder form was added to 30 g of deionized water and mixed for 20 minutes with a magnetic stirrer. After stirring and obtaining a concentrated solution of COC paste, pH was measured using a pH meter, OAKTON PC 300. The pH meter was calibrated at three points (pH of 4.01, 7.01, and 10.01) before each measurement age. pH for each mixture was measured once.

3.3.4 Setting Time

COC mortars of the following mixtures were prepared for setting time measurement: CO3-DBM, CO4-DBM, CO5-DBM, CO6-DBM, CO7-DBM, CO7-HYB, CO7-C$\overline{S}$A, and CO8-DBM. Setting times of COC mortars with different mixture ratios were measured using a Vicat needle apparatus. The experimental setup was modified from ASTM C807 (2021). Cylinder molds of 25 mm diameter and 50 mm height

were used as molds. While making the mortars, a W/B of 0.35 was used. Setting time for each mixture was measured once.

3.3.5 Thermogravimetric Analysis – Differential Scanning Calorimetry

Thermogravimetric analysis (TGA) and simultaneous differential scanning calorimetry (DSC) were carried out in the Central Laboratory of Middle East Technical University. The experiments were performed using an SDT650 simultaneous thermal analyzer in a nitrogen atmosphere by heating the samples to 800 °C at a rate of 15 °C per minute. Paste samples were prepared (CO7-DBM, CO7-HYB, CO7-C$\overline{S}$A) and cured similarly to the ones used for pH measurement and tested at 1 and 28 days.

3.3.6 Scanning Electron Microscopy

Scanning electron microscopy (SEM) analyses were performed in the Central Laboratory of Middle East Technical University to investigate the microstructure of COC pastes. The paste samples used in SEM were made of CO7-DBM, CO7-HYB, and CO7-C$\overline{S}$A mixtures and were cured similarly to the ones used for pH measurement. Images were taken at several magnifications at 1 and 28 days.

3.3.7 Mercury Intrusion Porosimetry

Mercury intrusion porosimetry (MIP) was used to characterize the pore structure of COC. In this technique, a non-wetting fluid (e.g., mercury) intrudes into the porous sample by applying increasing pressure (Scrivener et al., 2016). Cylinder-shaped pellet samples with approximately 0.7 cm diameter and 1 cm height were prepared and sent to METU Central Laboratory for testing. Similar to TGA and SEM experiments, the pastes of CO7-DBM, CO7-HYB, and CO7-C$\overline{S}$A were used when preparing COC pellets and were tested only at 28 days. Specimens prepared for MIP

were carefully cured by halting their contact with air and avoiding possible carbonation. Preventing carbonation on the sample surface is more critical in the case of MIP since carbonation might directly affect permeation and lead to misleading results.

The contact angle between mercury and porous surface (θ) and surface tension of mercury (γ) were taken as 140 ° and 0.48 N/m, respectively. The pressure (P) was applied up to 30,000 psi, a generic number for MIP applications in cementitious materials. This pressure theoretically enables measuring pore diameter (d) as small as 1.8 nm according to the Washburn equation (Equation 3.1), which is sufficient to demonstrate the distribution of capillary pores whose diameter is at least 10 nm (Dong et al., 2017).

$$d = -\frac{4\gamma \cos\theta}{P} \tag{3.1}$$

3.3.8 Coffee Cup Temperature Measurement

Pastes made with CO3-DBM, CO5-DBM, CO7-DBM, CO7-HYB, and CO7-C$\overline{S}$A mixtures were used. The pastes were mixed inside polystyrene coffee cups while the data logger recorded the temperature per second with type T thermocouples. W/B 0.3 was used in the preparation of paste samples. Each paste was prepared so that the total weight in a coffee cup was 26 g. For example, 14 g of CO, 6 g of DBM, and 6 g of water were mixed to prepare the temperature measurement paste of CO7-DBM. First, water was added to CO powder and mixed for 60-80 seconds; then, the other powder (DBM, C$\overline{S}$A, or their blend) was put in the mixture.

Figure 3.6a shows the experimental setup. The styrofoam cups used in the experiment (Figure 3.6b) were 4 and 7 cm in diameter at the bottom and top, respectively. To ensure insulation, coffee cups were closed with polystyrene lids with small holes that make room for mixing. Mixing holes were plugged with corks

to limit the amount of heat escaping after mixing was complete. Agilent 34972A data acquisition device was used in the experiment.

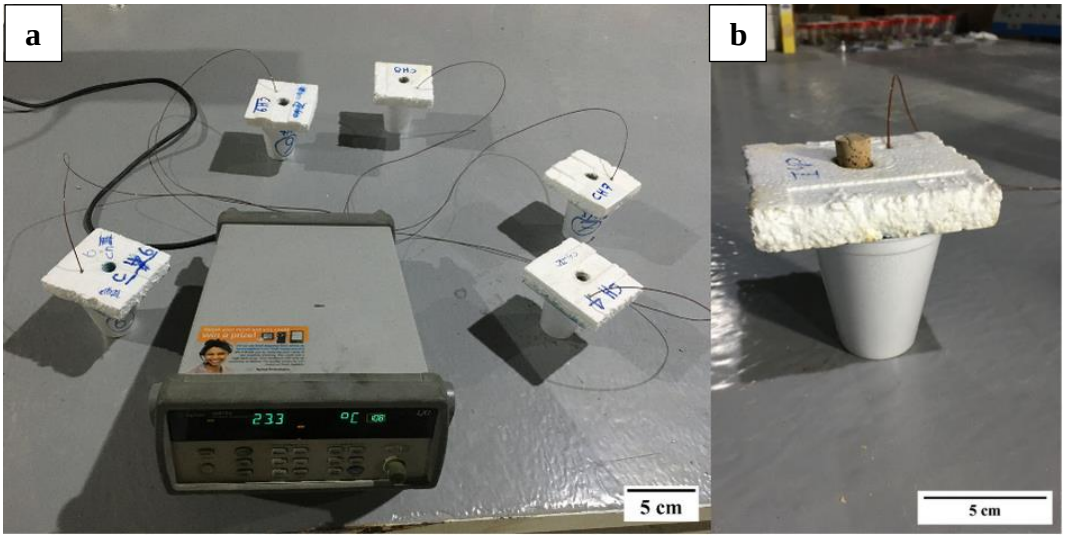

Figure 3.6 (a) The experimental setup for temperature measurement. The data logger is in the middle, and the cups with the COC pastes inside. (b) Close-up of a measurement cup showing the thermocouple wire and mixing hole plug.

3.3.9 Water Resistance

Cube mortar specimens with an edge length of 5 cm were air cured at room temperature for 28 days. Afterward, the specimens were immersed in containers filled with deionized water. The water inside the containers was not refreshed throughout the experiment. The containers were sealed with plastic foil to prevent the dissolution of CO_2 into the water and subsequent carbonation of the samples. The specimens were kept under water for 1, 7, and 28 days and their compressive strengths were measured immediately after removing from the water and drying their surfaces. An image of the setup can be seen in Figure 3.7 below.

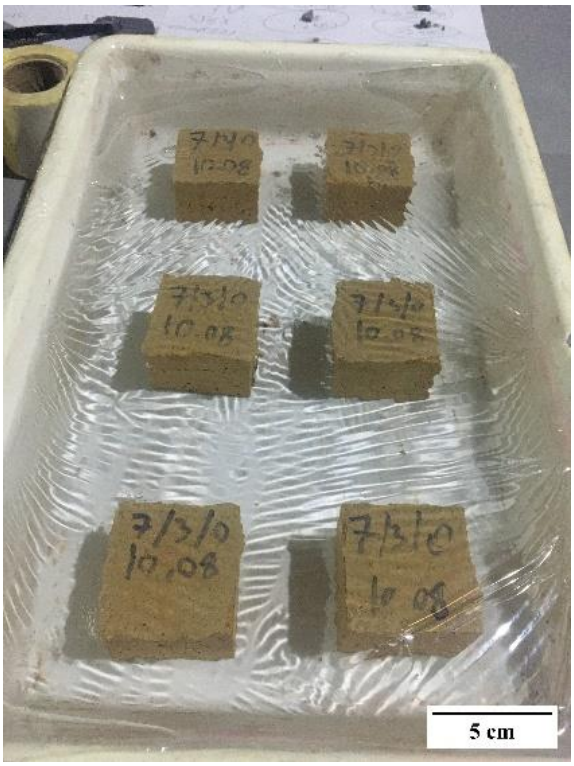

Figure 3.7 The experimental setup for water resistance testing. 5-cm COC mortar cube specimens are underwater.

CHAPTER 4

RESULTS AND DISCUSSION

The results of the experiments explained in Chapter 3 are presented and discussed in this chapter.

4.1 Determination of S/B in COC Mortars

As S/B increased, the workability of the mortar decreased. Poor workability led to defects in the surface texture of 5-cm cube mortar specimens due to difficulties during compaction. Figure 4.1 shows that the surface of the specimen of S/B=2.50 is smoother than those with S/B of 2.75 and 3.00. 1-day compressive strengths of mortars with an S/B ratio of 2.50, 2.75, and 3.00 were measured to evaluate the effect of the S/B ratio on strength. The results were 24.0, 23.5, and 24.4 MPa, respectively. S/B=2.50 was selected for mortars because the strengths did not differ much from one another, and the mortar with the S/B of 2.50 was the most workable one.

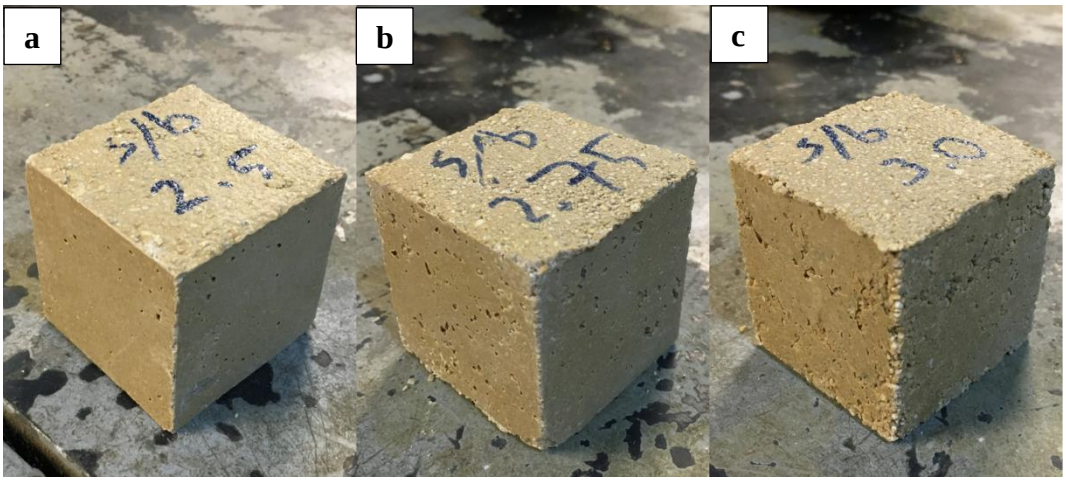

Figure 4.1 Visual change in the surface texture of 5-cm cubic mortar specimens for S/B of (a) 2.50, (b) 2.75, and (c) 3.00.

4.2 Compressive Strength

4.2.1 Influence of W/B on the Compressive Strength of MCO Mortars

The effect of the W/B on the compressive strength of CO7-DBM is shown in Figure 4.2. The compressive strength drops with increasing W/B, as expected. Due to workability problems, experiments did not cover a W/B lower than 0.35. From 7d to 28d, strengths decreased in mortar specimens with W/B of 0.40 and 0.45, probably due to the cement matrix being highly porous after excess water escaped.

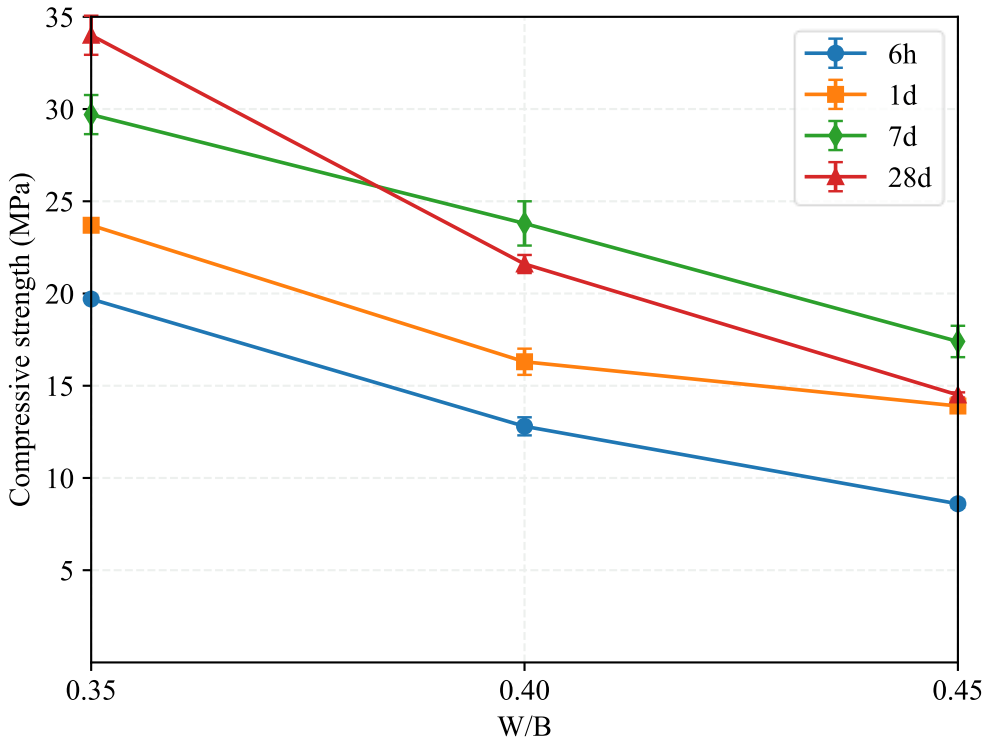

Figure 4.2 The change in compressive strength of CO7-DBM for changing W/B. Error bars show the standard deviation in strength.

4.2.2 Influence of CO/DBM on the Compressive Strength of MCO Mortars

Figure 4.3 depicts the change in compressive strength of the MCO mortars with changing CO/DBM. The MCO mortars of CO3-DBM, CO4-DBM, and CO5-DBM mixtures underperformed both in early and late strength compared to CO6-DBM, CO7-DBM, and CO8-DBM mortars due to insufficient formation of strength-giving magnesium oxalate compounds. Although having comparable compressive strength with CO8-DBM mixture at 28d and CO6-DBM mixture at 7d, CO7-DBM mixture gave the highest compressive strength at all ages, which is why CO7-DBM, CO7-HYB, and CO7-C$\bar{S}$A mixtures were primarily investigated in this study.

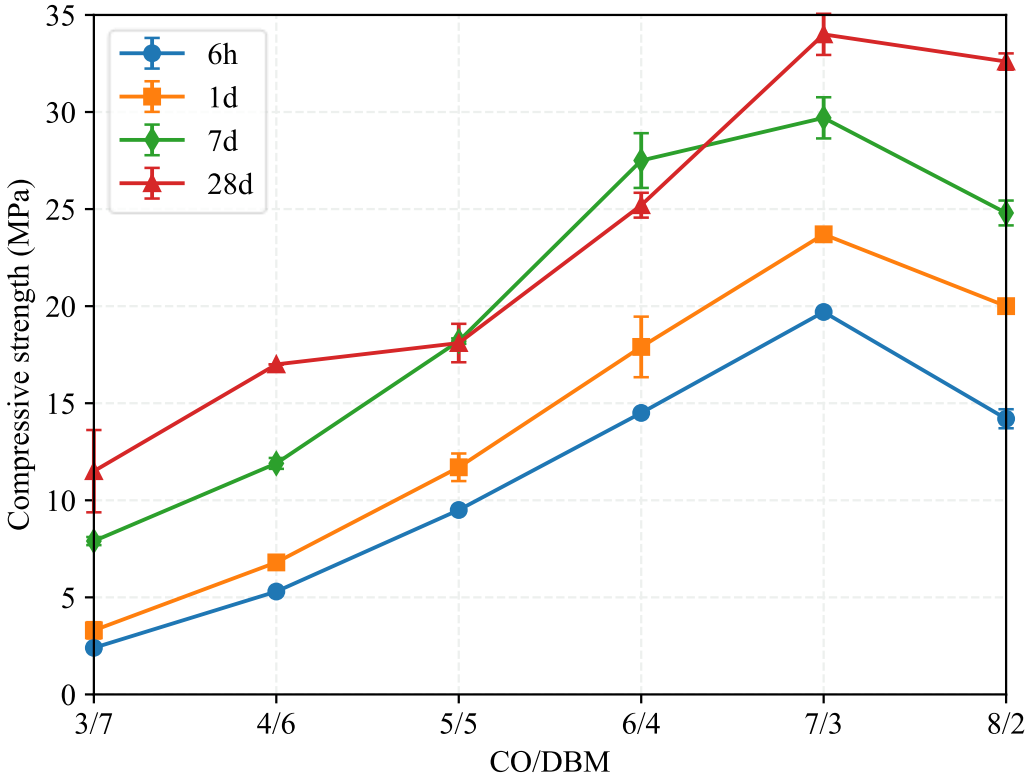

Figure 4.3 The change in the compressive strength of MCO specimens with varying CO/DBM. Error bars show the standard deviation in strength.

4.2.3 Influence of CO/C$\bar{S}$A on the Compressive Strength of C$\bar{S}$ACO Mortars

In Figure 4.4, the changes in compressive strength of the CO6-C$\bar{S}$A, CO7-C$\bar{S}$A, and CO8-C$\bar{S}$A mortars with varying CO/C$\bar{S}$A ratio are shown. Although 6h and 1d strengths tended to decrease with increasing CO/C$\bar{S}$A, this trend was not valid for strengths at 7d and 28d. Comparable 28d strengths around 25-30 MPa were achieved.

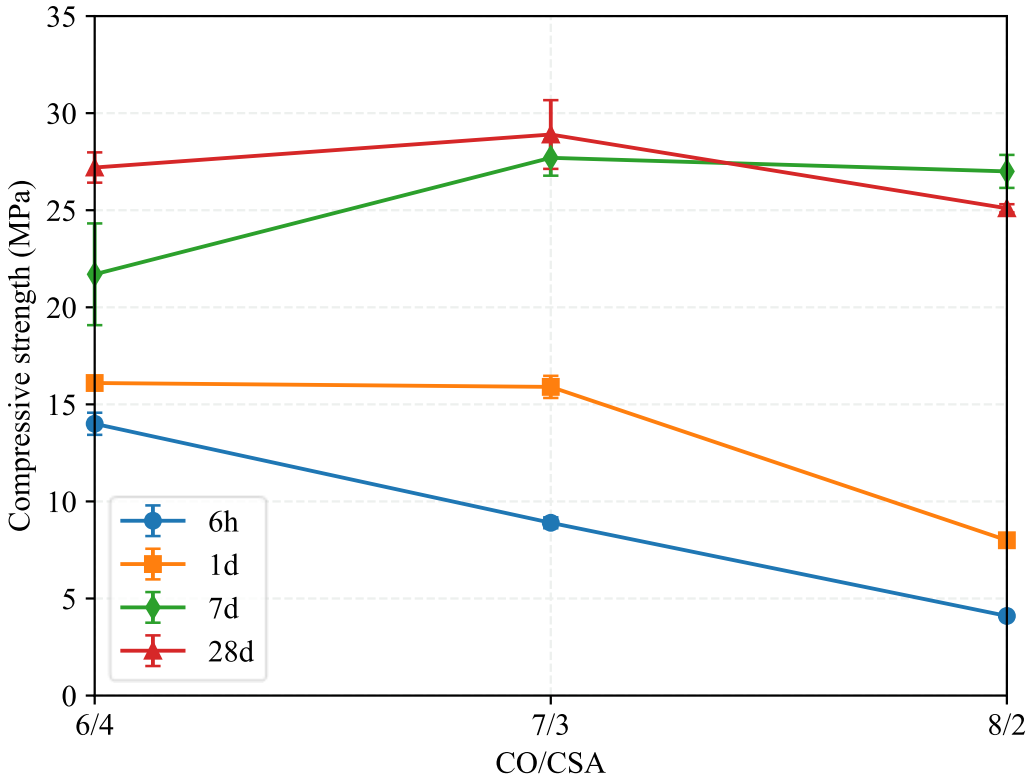

Figure 4.4 The change in the compressive strength of C$\bar{S}$ACO specimens with varying CO/C$\bar{S}$A. Error bars show the standard deviation in strength.

4.2.4 Influence of C$\bar{S}$A Clinker Replacement on the Compressive Strength of COC Mortars

In Figure 4.5, the strength development of the COC mortars prepared with CO6-DBM, CO6-HYB, and CO6-C$\bar{S}$A is shown. It can be observed that CO6-HYB

mortar gave higher strength than CO6-DBM and CO6-C$\bar{S}$A mortars at all ages. Although the other two are stronger at early ages, CO6-C$\bar{S}$A mixture reaches a comparable 28-day compressive strength, which might be a result of late activation of belite (C_2S) inside the incorporated C$\bar{S}$A clinker. As will be discussed in Section 4.3.4, ettringite ($C_6A\bar{S}H_{32}$) formation in the early ages does not occur; thus, COC mixtures could not benefit from the reaction mechanism giving early strength to C$\bar{S}$A cement.

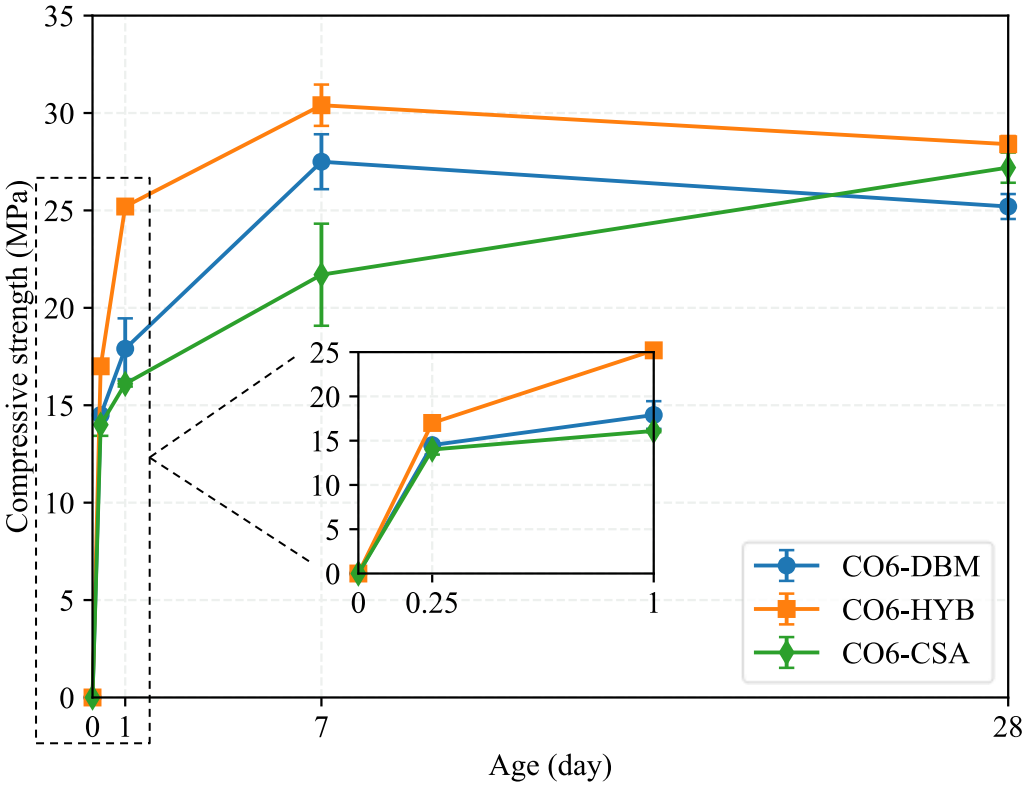

Figure 4.5 The strength development of the COC mortars of CO6-DBM, CO6-HYB, and CO6-C$\bar{S}$A. Error bars show the standard deviation in strength.

The strength development of the COC mortars prepared with CO7-DBM, CO7-HYB, and CO7-C$\bar{S}$A is shown in Figure 4.6. Unlike CO6-HYB, CO7-HYB does not show the highest compressive strength. Instead, CO7-DBM mortar gives the highest strength. Furthermore, although CO7-HYB mortar has higher compressive strength

than CO7-C$\bar{S}$A at 6h and 1d, they develop similar compressive strengths at later ages.

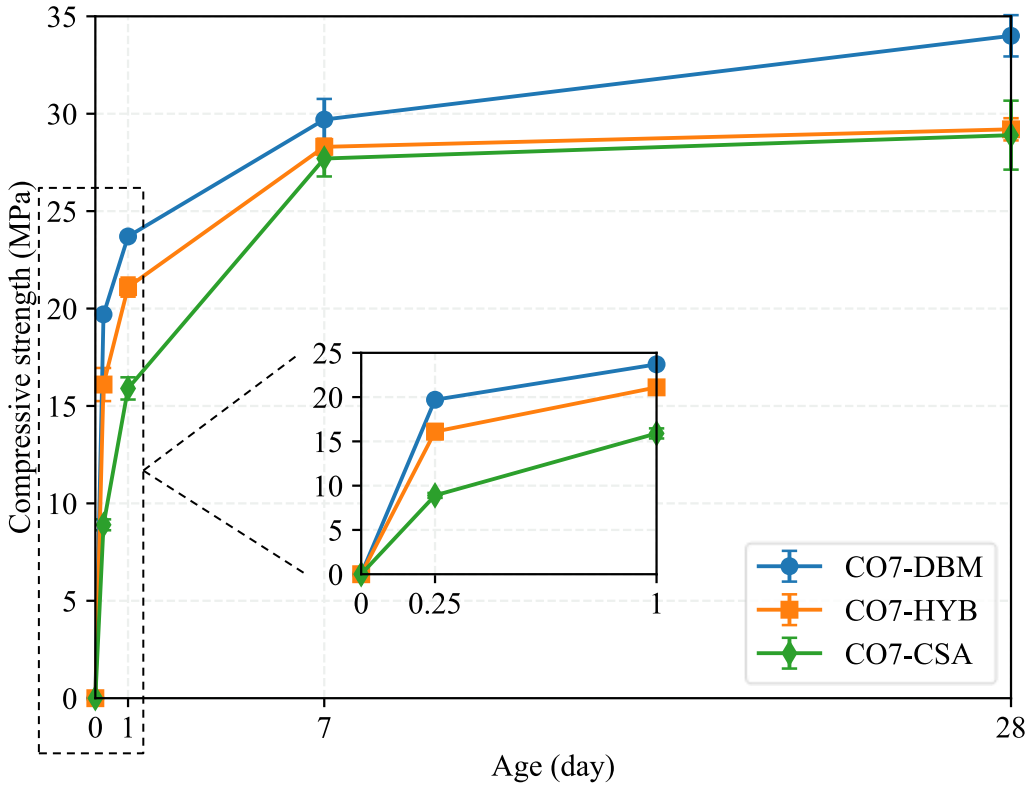

Figure 4.6 The strength development of the COC mortars of CO7-DBM, CO7-HYB, and CO7-C$\bar{S}$A. Error bars show the standard deviation in strength.

In Figure 4.7, the strength development of CO8-DBM, CO8-HYB, and CO8-C$\bar{S}$A specimens is displayed. CO8-DBM mortar cannot grow as strong as CO7-DBM in the early ages; however, 28-day strengths are comparable, CO7-DBM mixture having 34.0 MPa, and CO8-DBM mixture having 32.6 MPa. Additionally, CO8-C$\bar{S}$A mortar has significantly lower early strength than CO6-C$\bar{S}$A and CO7-C$\bar{S}$A mortars.

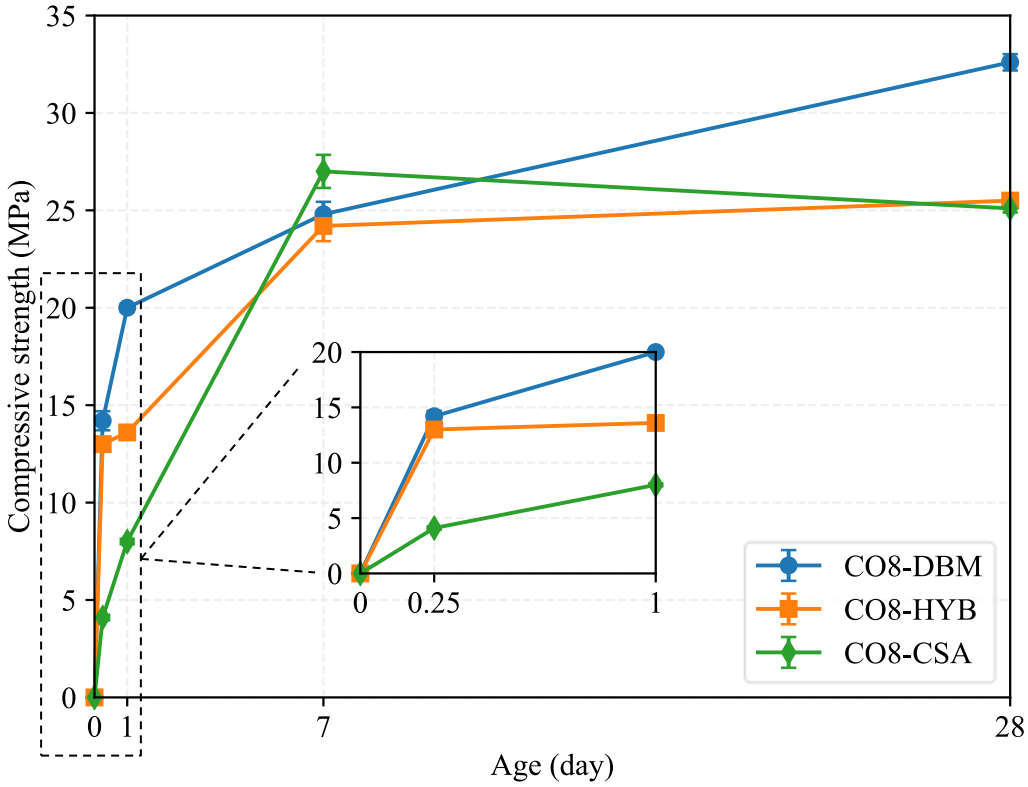

Figure 4.7 The strength development of the COC mortars of CO8-DBM, CO8-HYB, and CO8-C$\bar{S}$A. Error bars show the standard deviation in strength.

4.3 X-ray Diffraction Analysis

4.3.1 Influence of C/OA on the Crystal Structure of CO

Figure 4.8 presents the qualitative XRD analysis results for the CO powders with varying C/OA ratios. Many peaks of OA crystals (marked X on the figure) appear in the XRD pattern of CO-0.67 powder, which means that the intended partial neutralization of oxalic acid with clay was insufficient. The displayed OA peaks also match the observations in the preliminary trials made in the laboratory. The mixtures prepared with CO-0.67 were too warm and set too rapidly to handle, resulting from the OA left unreacted. On the other hand, CO-1.50 had low reactivity and did not get as warm as other mixtures while making a paste out of it.

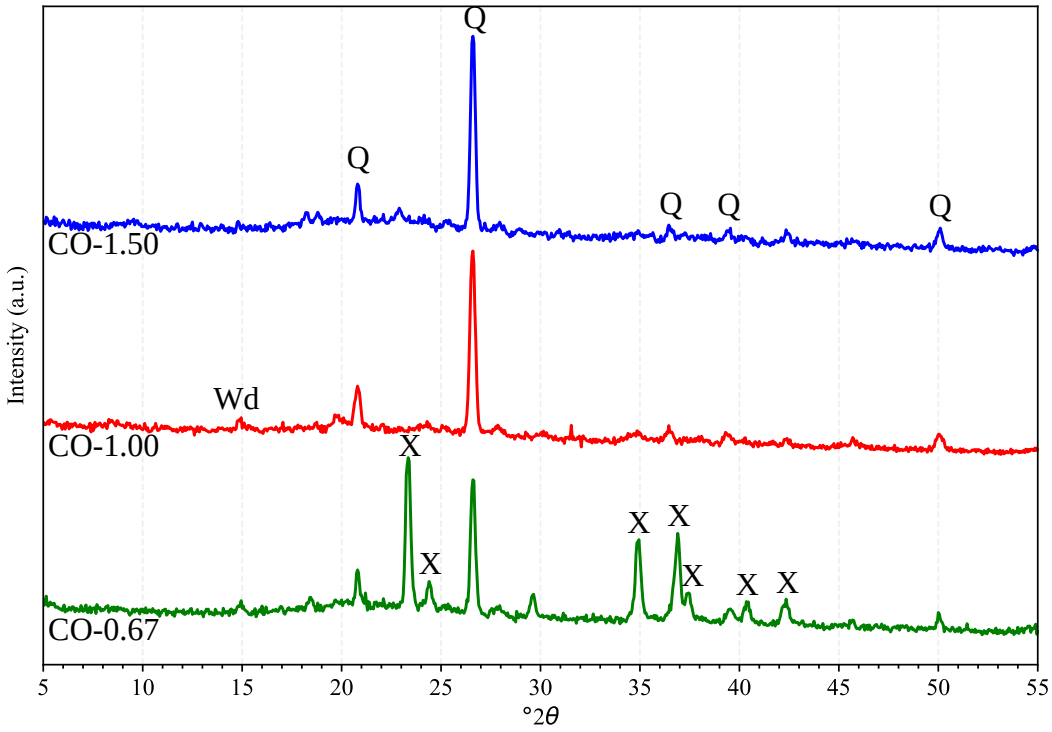

Figure 4.8 The XRD patterns observed in CO-1.50, CO-1.00, and CO-0.67. (Q: quartz, Wd: weddellite, X: oxalic acid)

Interestingly, although oxalate phases of metals (e.g., calcium, iron), such as whewellite ($CaC_2O_4 \cdot H_2O$), weddellite ($CaC_2O_4 \cdot (2+x)H_2O$) or humboldtine ($FeC_2O_4 \cdot 2H_2O$) were expected, there appears to be no sign of the formation of metal oxalate phases in the figure above, other than a little weddellite peak at around 15 °2θ in CO-1.00 sample. However, the pastes and mortars made with CO-1.00 warmed up and gained strength. From these findings, it can be said that the clay compounds react with OA to form amorphous products that cannot be seen by the XRD technique.

4.3.2 Influence of Calcination on the Crystal Structure of Magnesia

The XRD patterns before and after the calcination of magnesia at 1500 °C are plotted in Figure 4.9. The periclase (MgO) peaks remain unchanged after the dead-burning

process. The magnesite ($MgCO_3$) peaks, on the other hand, disappeared due to the decomposition of CO_2. Simultaneously, the formation of the forsterite (Mg_2SiO_4) crystals are observed due to SiO_2 impurities in the magnesia.

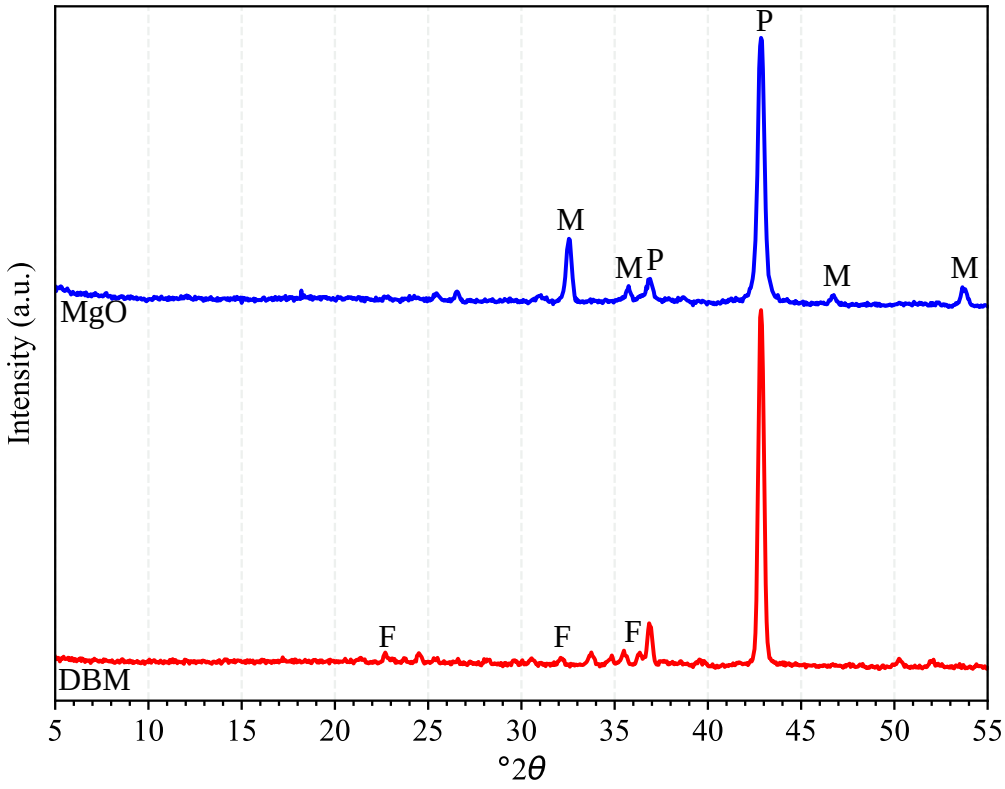

Figure 4.9 The XRD patterns observed in uncalcined MgO and DBM. (P: periclase, M: magnesite, F: forsterite)

4.3.3 Influence of the Change in CO/DBM Ratio on the Crystal Structure of MCO Pastes with Age

The diffraction patterns of MCO pastes from XRD analysis are shown in Figure 4.10. The formation of the magnesium oxalate phase, glushinskite ($Mg(C_2O_4)\cdot 2H_2O$) is observed in all mixtures at all ages. It can be noticed that as the periclase peak at around 43 °2θ becomes less intense with decreasing DBM proportion, the glushinskite peak at around 18 °2θ gets sharper. Glushinskite peaks could not grow more intense in the mixtures with lower DBM proportions because the oxalate ions

in the solution were insufficient. The inert quartz peaks also become more intense with increasing CO proportion. It should also be noted that despite the shortage of oxalate ions compared to magnesium cations in CO3-DBM and CO5-DBM pastes, glushinskite peaks could have been sharper if less calcined and more reactive magnesia had been used. However, the reaction rate would have been higher in such a case, hence would have led to lower setting times.

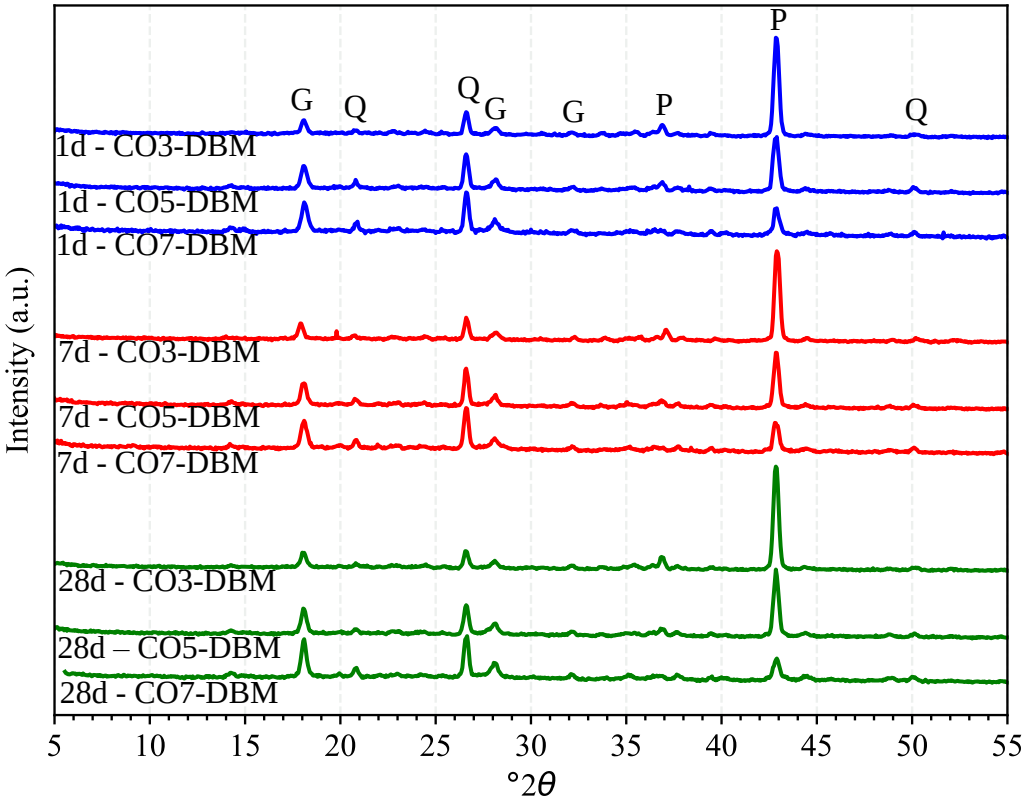

Figure 4.10 The XRD patterns of CO3-DBM, CO5-DBM, and CO7-DBM pastes at 1d, 7d, and 28d. (G: glushinskite, Q: quartz, P: periclase)

4.3.4 Influence of Replacing DBM with C$\bar{S}$A Clinker on the Crystal Structure of COC Pastes

Figure 4.11 below presents the XRD patterns of CO7-DBM, CO7-HYB, and CO7-C$\bar{S}$A pastes on the 1st, 7th, and 28th days of hydration. Glushinskite, quartz, and unreacted periclase are observed in CO7-DBM sample, as discussed in Section 4.3.3.

Glushinskite peaks get more intense as periclase peaks become less. Trace amounts of ettringite (peaks at ~9 and ~16 °2θ) are observed in mixtures including C$\bar{S}$A clinker beyond 7 days of hydration. It can be noticed that ettringite does not form in appreciable amounts and ye'elimite, which is consumed in the early stages of its hydration to form ettringite, remains on the 28th day of hydration.

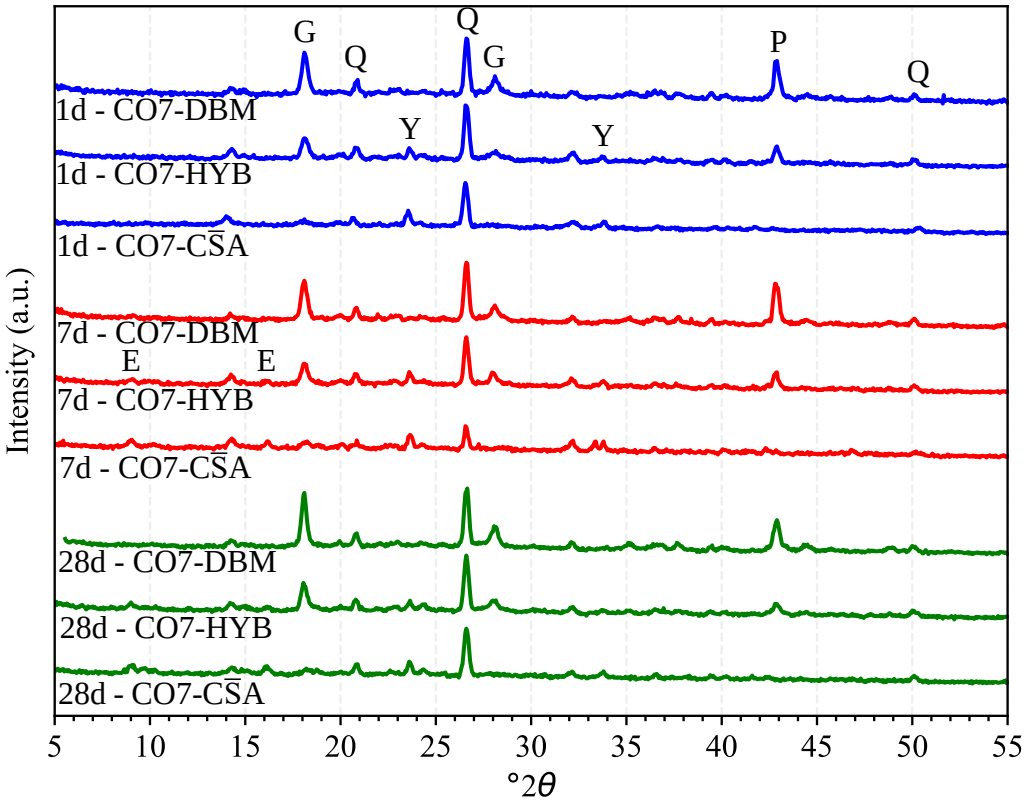

Figure 4.11 The XRD patterns of CO7-DBM, CO7-HYB, and CO7-C$\bar{S}$A pastes at the ages of 1, 7, and 28 days. (G: glushinskite, Q: quartz, P: periclase, Y: ye'elimite, E: ettringite)

4.4 Setting Time

The penetration depths of the Vicat needle recorded every two minutes for COC mortars with different CO/DBM ratios are visualized in Figure 4.12. The figure can be used to illustrate the initial and final setting times of COC. For an individual curve,

the first sharp drop in penetration depth may be regarded as the indicator of the initial set, while the final set is observed during the second drop in that curve's slope.

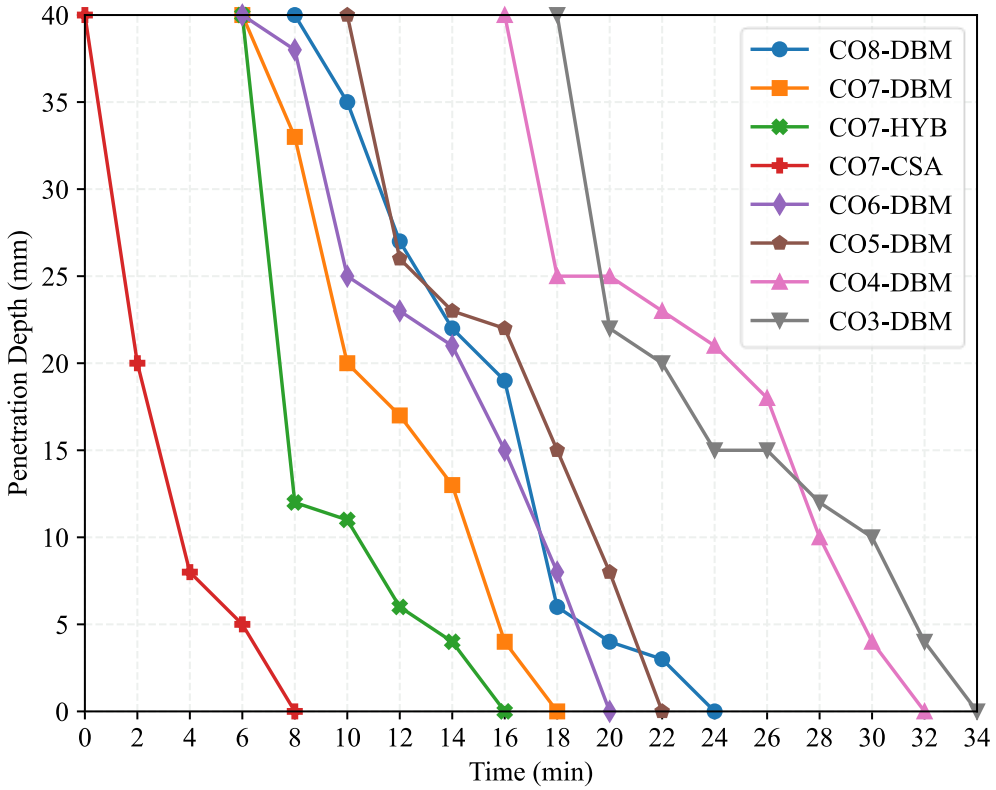

Figure 4.12 Penetration depth of Vicat needle for various COC mortars.

In ASTM C807 (2021), the following equation (Equation 4.1) for calculating setting time is recommended:

$$\left(\frac{\text{H-E}}{\text{C-D}}\times(\text{C-10})\right)+\text{E} \tag{4.1}$$

where *E* is the time in minutes of the last penetration larger than 10 mm, *H* is the time in minutes of the first penetration less than 10 mm, *C* is the penetration reading at time *E*, and *D* is the penetration reading at time *H*. Although ASTM C807 (2021) standard was modified during the experiments in this study, the suggested equation for calculating setting time yields the values listed in Table 4.1.

Table 4.1 Setting times of COC mortars.

Mixture	Setting time (min)
CO3-DBM	29
CO4-DBM	28
CO5-DBM	19
CO6-DBM	17
CO7-DBM	15
CO7-HYB	10
CO7-C$\overline{S}$A	4
CO8-DBM	17

CO3-DBM and CO4-DBM mortars set in noticeably longer times than the others. Setting times get shorter as the CO dosage increases up to 70 wt. % of the total powder in the mixture. CO8-DBM mortar set 2 minutes later than CO7-DBM mortar, probably because DBM was not adequate to react with all oxalate ions. Moreover, substituting DBM with C$\overline{S}$A led to a more rapid setting. CO7-HYB and CO7-C$\overline{S}$A mortars set in 10 and 4 minutes, respectively, while the setting time of CO7-DBM mortar was 15 minutes.

4.5 pH Measurement

pH measurement results for COC pastes prepared with CO7-DBM, CO7-HYB, and CO7-C$\overline{S}$A are presented in Figure 4.13. It can be noticed that CO7-DBM mixture displays a more alkaline behavior than CO7-HYB, whereas CO7-C$\overline{S}$A remains in the acidic range at all ages. Aligned with the XRD analysis results, it can be inferred that glushinskite (magnesium oxalate dihydrate, $MgC_2O_4 \cdot 2H_2O$) forms in CO7-DBM, while glushinskite is not observed for CO7-C$\overline{S}$A paste, which suggests that the formation of glushinskite consumes oxalate ions and leads to an alkaline cementitious matrix. Moreover, C$\overline{S}$A hydration products, which normally lead to an alkaline matrix with a pH of at least 11.5 (Odler, 2000), did not form; thus pH of the

solution of CO7-C$\bar{S}$A paste does not go above 6. This may be explained by the absence of gypsum/anhydrite in the system to form ettringite. C-S-H products may not also be forming in such an acidic medium because C-S-H is unstable at pH < 9.5 (Bernard et al., 2017).

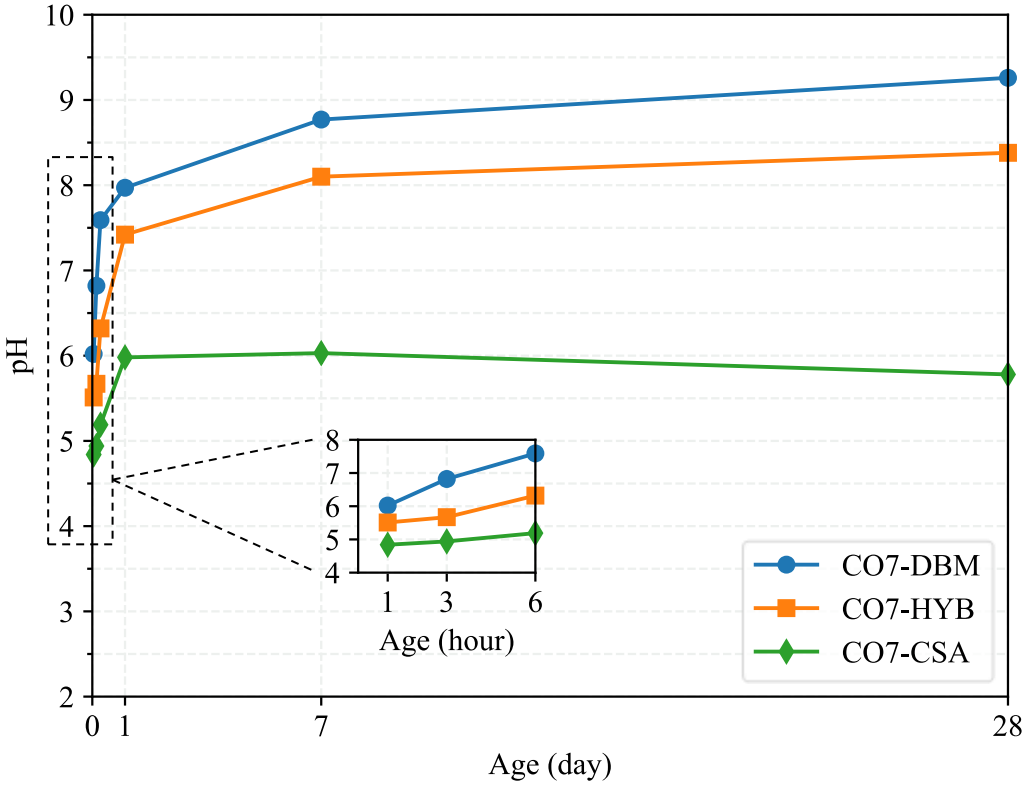

Figure 4.13 pH measurement results for COC pastes prepared with CO7-DBM, CO7-HYB, and CO7-C$\bar{S}$A.

4.6 Thermogravimetric Analysis

The thermogravimetric analyses of CO7-DBM, CO7-HYB, and CO7-C$\bar{S}$A pastes at 1 and 28 days after hydration are presented in Figure 4.14 and Figure 4.15, respectively. In Figure 4.14a, there are two main mass losses for the 1-day CO7-DBM and CO7-HYB pastes. According to Mastuli et al. (2014), the dehydration of magnesium oxalate dihydrate ($MgC_2O_4 \cdot 2H_2O$, glushinskite) occurs between 160 °C and 240 °C, causing two endothermic peaks at 180 °C and 210 °C. The first main

mass loss around 200 °C can be affiliated with the dehydration of glushinskite. Moreover, Mastuli et al. (2014) also mention that between 400 °C and 510°C, the decomposition of remaining magnesium oxalate to magnesite ($MgCO_3$) and carbon monoxide, and the decomposition of magnesite to magnesium oxide and carbon dioxide take place, respectively. Thus, the second main step between 400 °C and 500 °C accounts for the decomposition of magnesium oxalate.

Some endothermic peaks in Figure 4.14b could not be identified precisely. The curves of CO7-C$\overline{S}$A and CO7-HYB pastes have two endothermic peaks at around 60 °C and 160 °C, which might have been attributed to the presence of ettringite if it was detected in XRD analyses. Moreover, Curetti et al. (2022) state that the thermal decomposition of calcium oxalate hydrates (e.g., whewellite or weddellite) occurs in three temperature ranges. The first is observed at 70 - 200 °C, with the maximum weight loss rate at 136 °C, while the second is at 390 - 550 °C with a maximum weight loss rate at 490 °C, and the third is at 550 - 800 °C with the maximum rate at 767 °C. In Figure 4.14b, the three endothermic peaks of CO7-DBM and CO7-HYB pastes at 160 °C, 390 °C, and 690 °C might be of the gradual decomposition of calcium oxalate hydrate ($CaC_2O_4 \cdot H_2O$) to first calcium oxalate anhydrite (CaC_2O_4), then to calcium carbonate ($CaCO_3$, calcite), and finally to calcium oxide and carbon dioxide, respectively. The temperature ranges that these mass losses observed comply with Curetti et al. (2022); however, calcium oxalate compounds were not found in XRD analyses. Furthermore, the temperatures at which the weight loss rates peak are not exactly the same. Therefore, these results cannot prove the existence of calcium oxalates. Nevertheless, the weight losses near 700 °C probably indicate that calcium carbonates exist in the pastes made with C$\overline{S}$A. Finally, although CO7-C$\overline{S}$A paste goes through weight loss between 420 °C and 500 °C, it remains unknown, and undoubtedly not due to the presence of magnesium oxalates.

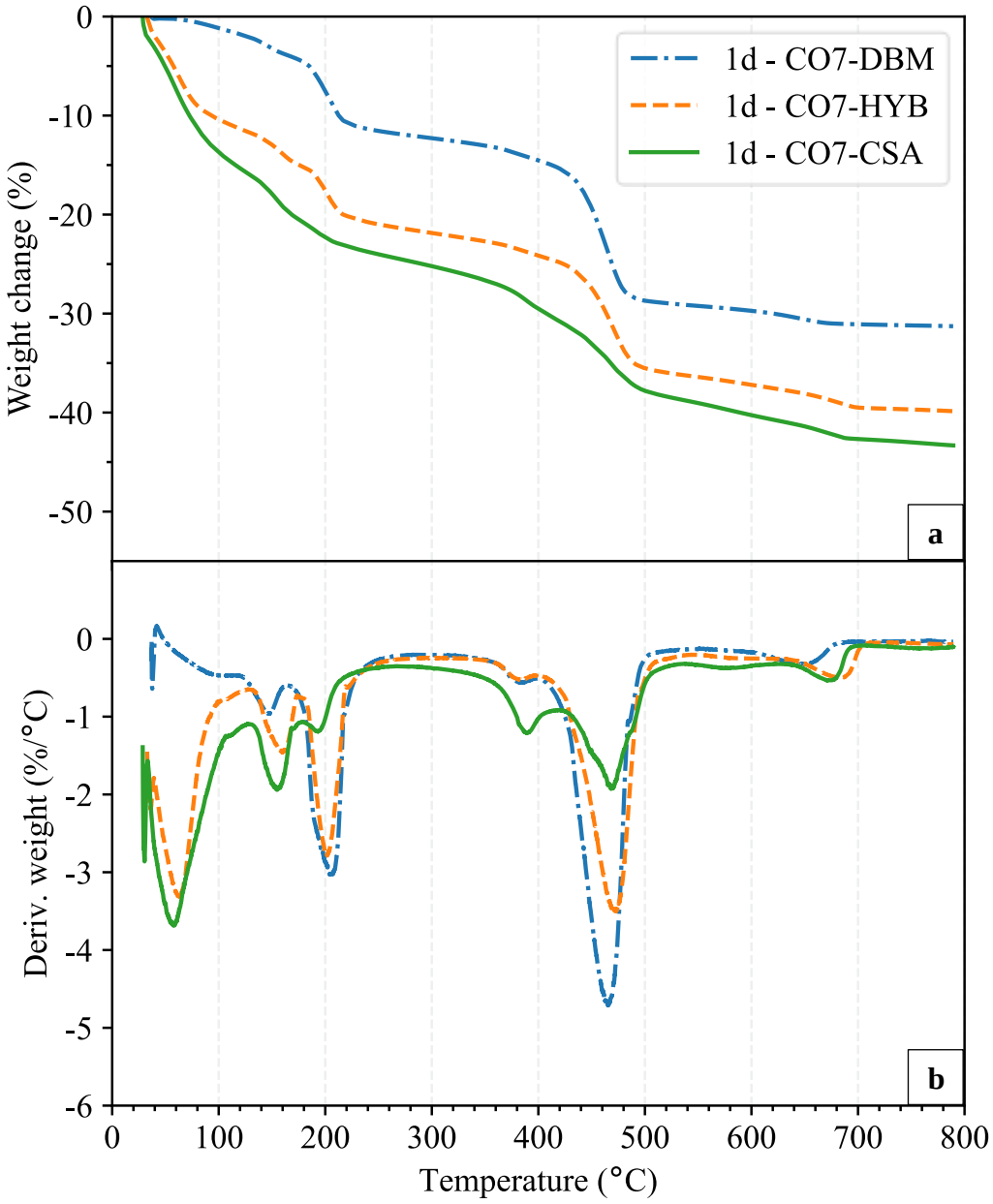

Figure 4.14 Thermogravimetric analysis of CO7-DBM, CO7-HYB, and CO7-C$\bar{S}$A pastes at 1d.

In Figure 4.15a, the thermal analyses of 28-day COC samples show similar results to the 1-day samples. Two major steps in weight loss are observed at the same temperatures as the 1-day sample. Hence, the presence of magnesium oxalates is noticeable. Different than what was observed in the 1-day sample, another endothermic peak can be seen at around 450 °C on the 28th day of hydration of CO7-C$\overline{S}$A paste. Scrivener et al. (2016) say that the decomposition of portlandite ($Ca(OH)_2$) occurs at 450 °C. On that account, the newly-emerged weight loss at 450 °C is an indication of late C_2S hydration, which produces amorphous reaction products, C-S-H, and portlandite. Scrivener et al. (2016) also mention that below 600 °C, amorphous reaction products and C-S-H undergo thermal decomposition continuously.

To summarize this section, magnesium oxalate compounds are observed in the presence of magnesium. Although ettringite formation was expected due to the hydration of ye'elimite coming from C$\overline{S}$A clinker, it was not observed in CO7-C$\overline{S}$A and CO7-HYB pastes. Besides, late hydration of belite coming from C$\overline{S}$A clinker provides amorphous reaction products and C-S-H to the matrix.

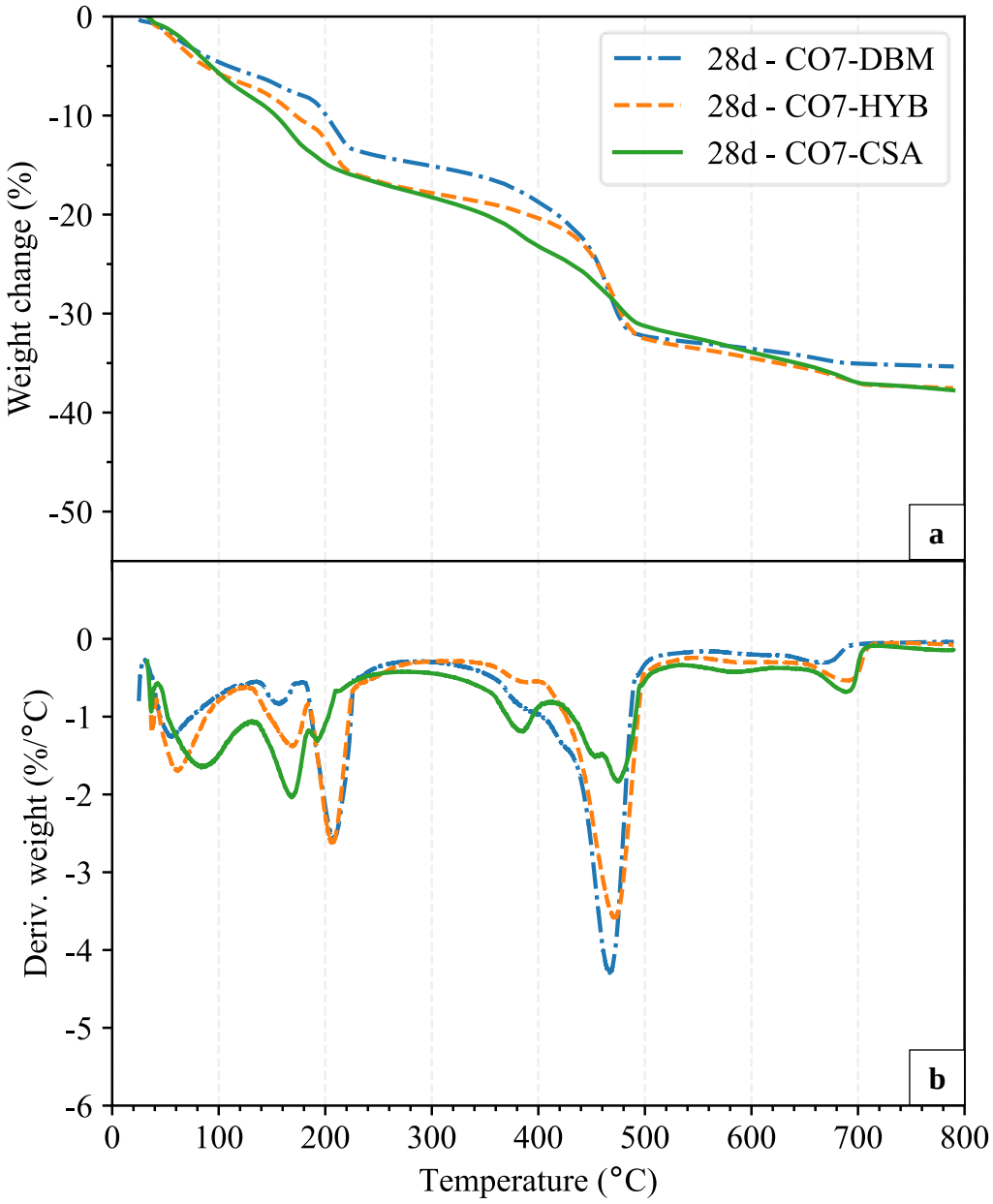

Figure 4.15 Thermogravimetric analysis of CO7-DBM, CO7-HYB, and CO7-C$\bar{S}$A pastes at 28d.

4.7 Scanning Electron Microscopy

SEM images of CO7-DBM paste samples at 1d and 28d are presented in Figure 4.16. The particle tagged as "1a1" is unreacted magnesia. Although the zoom is not sufficient, small cube-shaped early hydration products of MCO paste ("1b1") may be glushinskite. The hardened paste medium of 28-day MCO paste ("1c1" and "1d2" areas) looks denser than that of the 1-day paste ("1b1" area). Smaller unreacted magnesia particles like the one tagged as "1d1" may indicate the magnesia consumption by magnesium oxalate reactions. Overall, the hardened paste medium is amorphous both in early and late ages, and not much crystal growth can be observed.

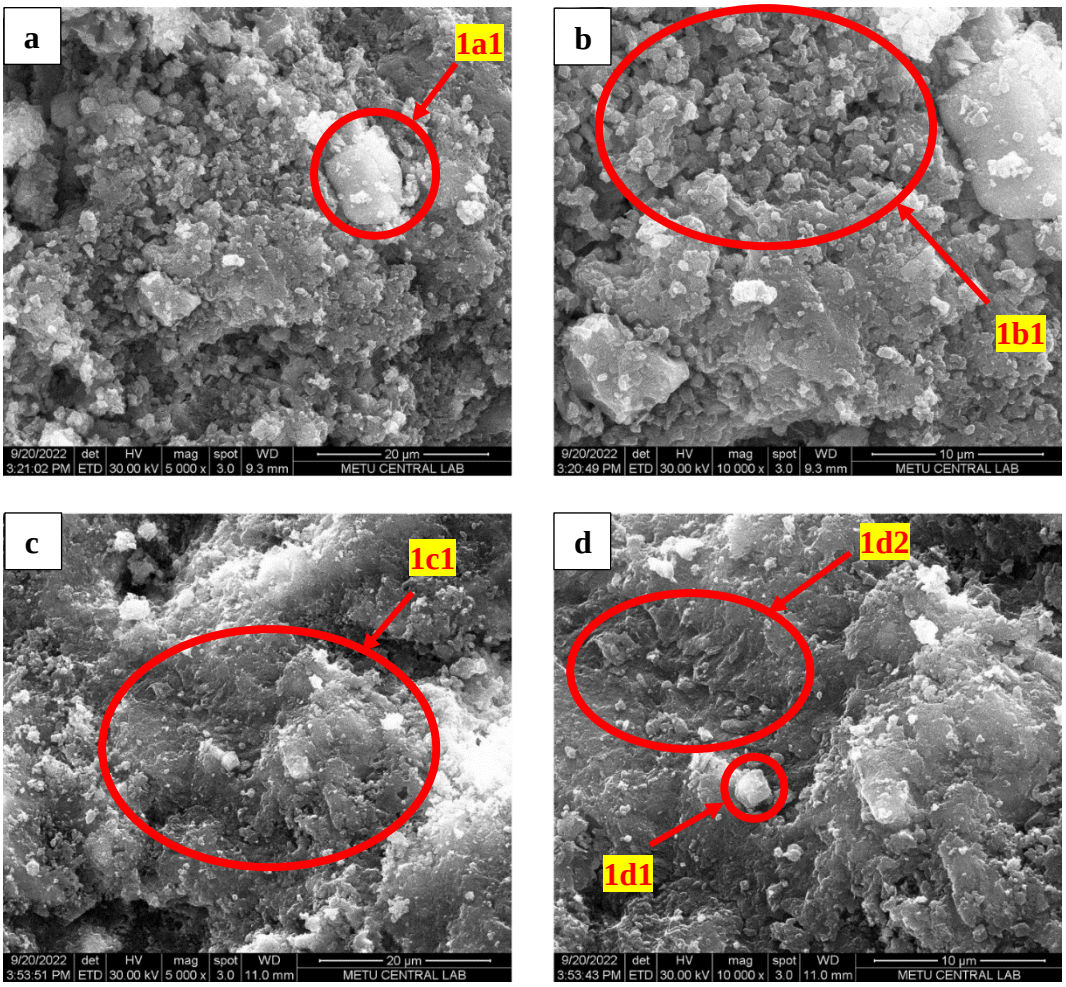

Figure 4.16 SEM images of CO7-DBM pastes at (a-b) 1d and (c-d) 28d.

SEM images of CO7-HYB paste samples at 1d and 28d are presented in Figure 4.17. The amorphous reaction products of 1-day CO7-HYB paste can be seen in the areas tagged as “2a1” and “2b1”. The amorphous reaction products of 28-day CO7-HYB paste are displayed inside “2c1” and “2d1”.

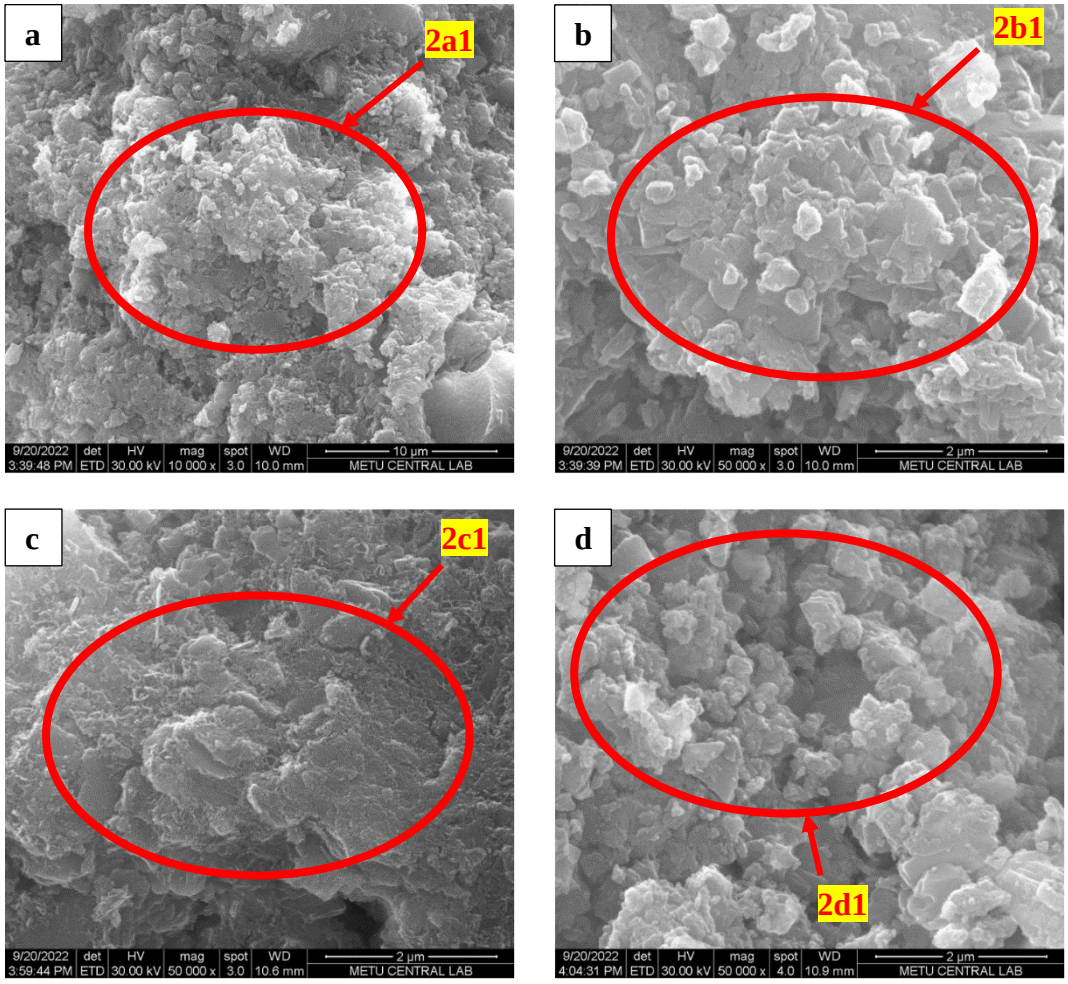

Figure 4.17 SEM images of CO7-HYB pastes at (a-b) 1 day and (c-d) 28 days.

SEM images of CO7-C$\bar{S}$A paste samples at 1d and 28d are presented in Figure 4.18a-b and Figure 4.18c-d, respectively. Ettringite occurrence may be observed inside the “3b1” area, zoomed-in image of the “3a1” area, which is the most explicit image of crystal growth in COC pastes obtained from SEM. The amorphous reaction products of 28-day CO7-C$\bar{S}$A paste are seen inside “3c1” and “3d1” circles.

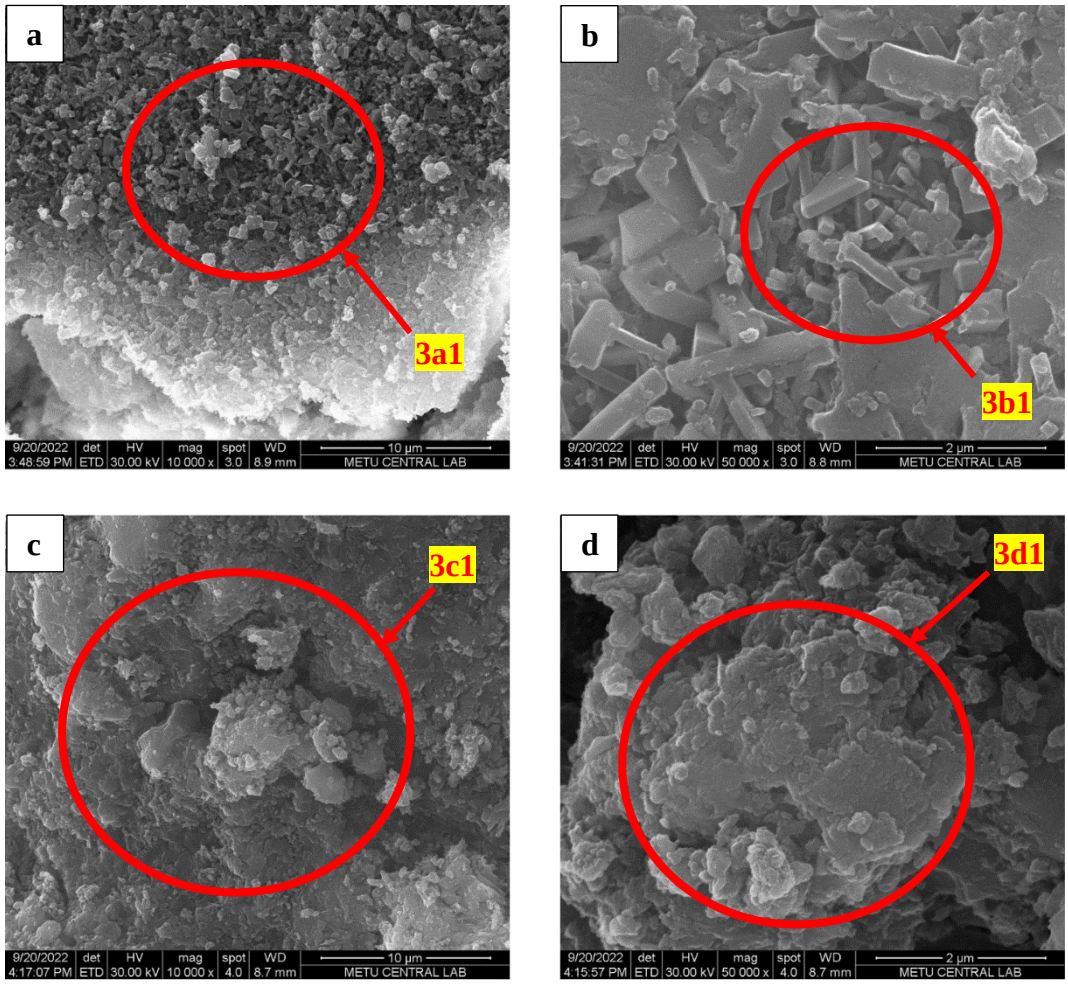

Figure 4.18 SEM images of CO7-C$\bar{S}$A pastes at (a-b) 1 day, and (c-d) 28 day.

4.8 Mercury Intrusion Porosimetry

Pore volume vs. pore diameter (cumulative porosity) and differential pore volume vs. pore diameter (pore size distribution) graphs are plotted in Figure 4.19a and Figure 4.19b, respectively. The difference between total pore volumes of COC pastes is relatively small. CO7-DBM and CO7-HYB pastes showed similar total pore volumes. The total pore volume of CO7-DBM paste was 10.3 %, and that of CO7-HYB paste was 10.5 %. The total pore volume of CO7-C$\bar{S}$A was found as 11.4 %. All these total porosity values are slightly lower than that of MgFAOx in the study of Erdoğan et al. (2022) and slightly higher than that of MKPC (M/P=8 and M/P=4.5)

in the study of Xu et al. (2017). In addition, the total porosity of COC pastes is nearly twice as low as OPC paste, three times as low as OPC incorporating ground steel slag or fly ash (Yong-xin et al., 2003; Zeng et al., 2012).

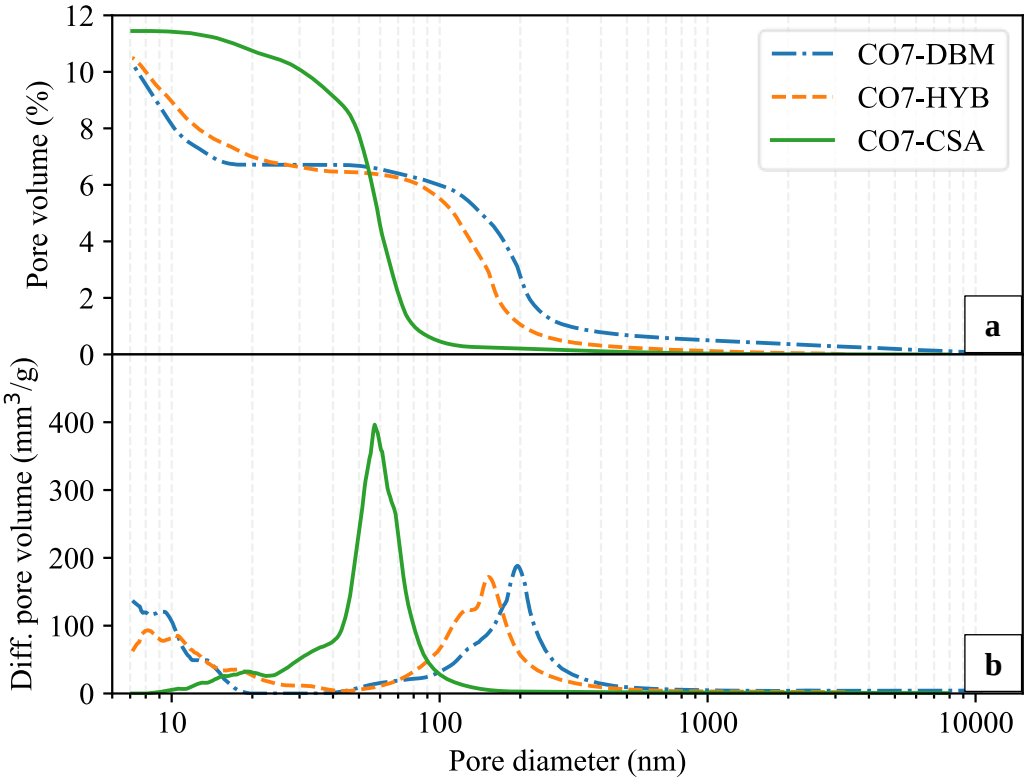

Figure 4.19 (a) Cumulative porosity and (b) pore size distribution of CO7-DBM, CO7-HYB, and CO7-C$\bar{S}$A pastes.

Although CO7-C$\bar{S}$A paste has a slightly higher total pore volume than the other two, it has a lower critical pore entry diameter (60 nm). The green dotted curves indicate that the majority of pores inside CO7-C$\bar{S}$A matrix are between 10 nm and 100 nm with an average pore entry diameter of 55 nm. The critical pore entry diameter of CO7-DBM was measured as 200 nm, whereas the critical pore entry diameter of CO7-HYB paste was about 150 nm. Different from what was observed in CO7-C$\bar{S}$A, CO7-DBM, and CO7-HYB display cumulative porosity curves with double inflection points. For CO7-DBM paste, a concentration of pore size distribution occurs in the ranges of 50-400 nm and 7-20 nm with an average pore entry diameter

of 110 nm, while such a concentration is observed between 60 and 300 nm and between 7 and 30 nm for CO7-HYB paste with average pore entry diameter of 76 nm. It should be noted that the minimum pore diameter measured by the instrument was 7 nm.

MIP has limitations due to the theoretical assumptions it is based on. The resulting pore size information is not a direct indicator of durability because the connectivity of pores cannot be measured. Kumar and Bhattacharjee (2004) investigated the correlation between the initial surface absorption rate and pore entry size of concrete matrix. They conclude that the permeability of concrete may be evaluated if pore structure characteristics are known. In that regard, MIP results presented above indicate that CO7-C$\overline{S}$A and CO7-HYB are expected to have lower permeation, thus, better durability than CO7-DBM due to smaller average pore entry size.

4.9 Coffee Cup Temperature Measurement

Figure 4.20 displays the coffee cup temperature measurements performed on COC pastes. CO3-DBM and CO5-DBM do not get as warm as others, staying just below 40 °C. While this means more workable mixtures than the higher-CO-containing ones, because temperature increase is an outcome of hydration reactions, the compressive strength development of the lower-CO mixtures is limited, according to the results in Section 4.2.2.

On the other hand, CO7-DBM and CO7-HYB pastes reach similar temperatures, around 40 °C upon hydrating CO and about 50 °C upon adding alkaline precursors, indicating that analogous hydration reactions occur in comparable amounts in these mixtures. Moreover, CO7-C$\overline{S}$A paste is clearly the hottest mixture of all, warming up to nearly 58 °C, which proves that the hydration mechanism of CO7-HYB paste is dominated by magnesium-based reactions, as otherwise would result in the temperature of CO7-HYB paste being closer to that of CO7-C$\overline{S}$A paste.

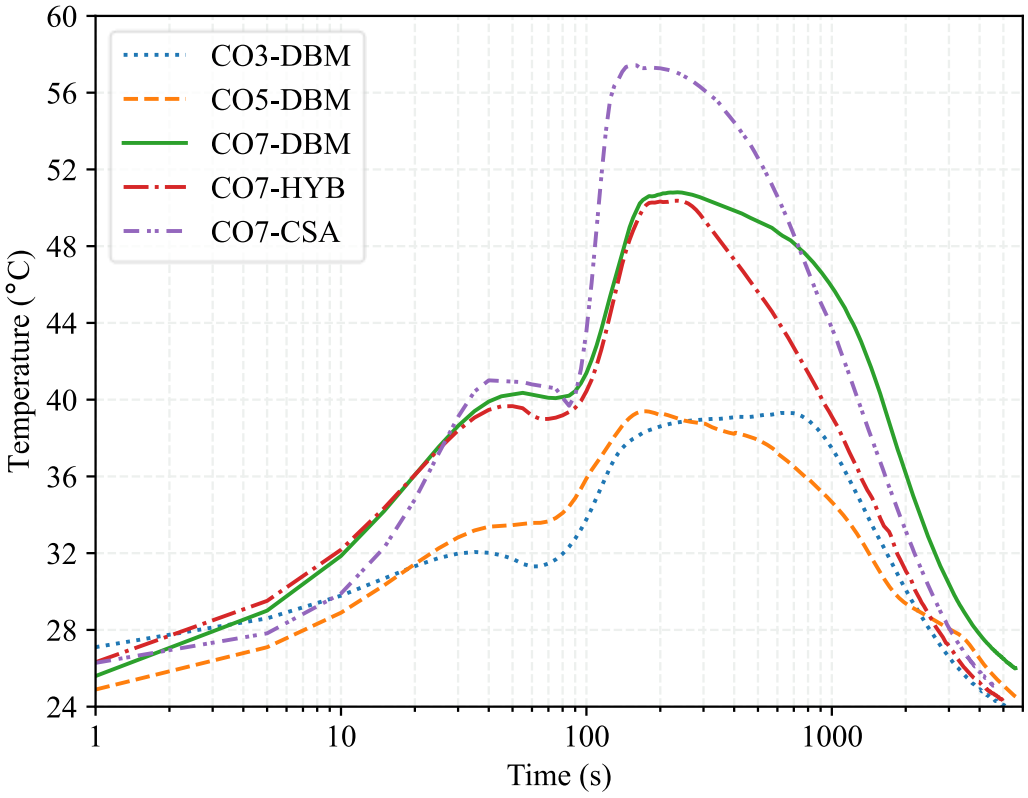

Figure 4.20 Coffee cup temperature measurement for COC pastes.

4.10 Water Resistance

The changes in the compressive strength of CO7-DBM, CO7-HYB, and CO7-C$\bar{S}$A after immersing them in water for 1, 7, and 28 days are shown in Figure 4.21.

1d after immersion, all mortar samples displayed a sharp decrease in compressive strength. CO7-DBM, CO7-HYB, and CO7-C$\bar{S}$A mortars lost 38 %, 29 %, and 28 % of their 28-day compressive strengths, respectively. The compressive strength of CO7-C$\bar{S}$A mortar did not significantly decrease further at the later ages of immersion. On the other hand, CO7-DBM and CO7-HYB mortars recovered their compressive strength in time. 28d after immersion, CO7-DBM and CO7-HYB mortars gave even higher compressive strength than measured before the immersion.

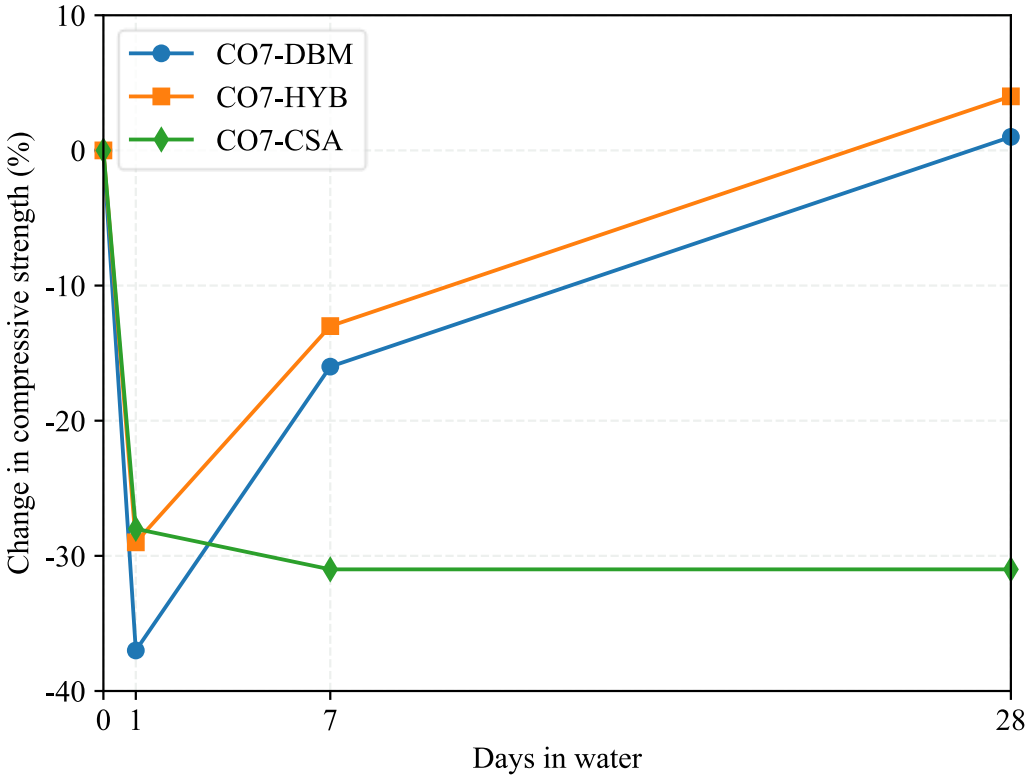

Figure 4.21 The change in compressive strength of CO7-DBM, CO7-HYB, and CO7-C$\bar{S}$A mortar specimens after immersed in water for 1, 7, and 28 days.

According to the results, the drop in compressive strengths of all mortar specimens 1d after being immersed might be due to the dissolution of high-solubility compounds in the matrix, as well as the presence of excess water in pores. Hydration of the space-filling solids that remained unhydrated could also be contributing to the decrease in strength. At 7 and 28d after immersion, the reaction between magnesium and oxalate ions continued in the pore solution of CO7-DBM and CO7-HYB mixtures. Consequently, CO7-DBM and CO7-HYB mortar specimens regained the compressive strength lost at the early ages of immersion. Besides, CO7-C$\bar{S}$A mortar specimens could not recover the negative change in their compressive strength.

4.11 Carbon Footprint Analysis for Optimal COC Mix Proportions

CF analysis of COC was made by relying on the data provided in Table 4.2 to suggest an optimal mix proportion. The emission data were retrieved from various life-cycle CO_2 studies (Hanein et al., 2018; Peñaloza Isidro et al., 2018; Zhao et al., 2022).

Table 4.2 CO_2 emission data of the materials used in the preparation of COC mixtures.

Material	**Process**	**CF ($kgCO_2/t$)**		**Reference**
		CO_2 emission	**Total**	
Dead-burned magnesia	Magnesite mining and roasting	~2200	2200	(Zhao et al., 2022)
Clay	Extraction	~3	5.5	(Peñaloza Isidro et al., 2018)
	Transportation	~2		
	Storage and grinding	~0.5		
Oxalic acid	Direct conversion from CO_2 (theoretical)	-978*	-978	Equation 2.7
$C\bar{S}A$	Raw material supply	~50	580	(Hanein et al., 2018)
	Limestone calcination	~350		
	Natural gas combustion	~180		

*Carbon capture feature of oxalic acid is counted as negative emission.

4.11.1 Optimal Mix Proportion Calculation for MCO Paste

Assuming CO is made with a Clay/OA ratio of 1, the weight of clay and OA are equal and half the weight of CO (W_{CO}). CF of CO (CF_{CO}) can be calculated as in Equation 4.2.

$$CF_{CO} = 5.5\times\frac{W_{CO}}{2} - 978\times\frac{W_{CO}}{2} \cong -486W_{CO} \qquad (4.2)$$

CF of DBM (CF_{DBM}) is $2200W_{DBM,}$ according to Table 4.2. For a carbon-neutral mixture, CF_{CO} and CF_{DBM} should be equal. The W_{CO}/W_{DBM} ratio to achieve a carbon-neutral MCO paste was calculated as 2200/486=4.52. Thus, a CO/DBM/C$\bar{S}$A ratio of 8.19/1.81/0.00 (close to the proportions of CO8-DBM) would make a zero-carbon paste. Increasing CO dosage would make a carbon-negative paste, but one can expect to observe lower strength and higher costs in such a case.

4.11.2 Optimal Mix Proportion Calculation for HYBCO Paste

CF_{CO} was calculated as $-486W_{CO}$ in Equation 4.2. Assuming a 50 % C$\bar{S}$A clinker substitution ratio, the weight of DBM and C$\bar{S}$A are equal and half the weight of total alkaline powder (W_{HYB}). CF of the alkaline powder (CF_{HYB}) can be calculated as in Equation 4.3.

$$CF_{HYB} = 2200\times\frac{W_{HYB}}{2} - 580\times\frac{W_{HYB}}{2} = 1390W_{HYB} \qquad (4.3)$$

For a carbon-neutral HYBCO mixture, CF_{CO} and CF_{HYB} should be equal. A carbon-neutral mixture can be obtained by employing a W_{CO}/W_{HYB} ratio of 1390/486=2.86, which is equivalent to a CO/DBM/C$\bar{S}$A ratio of 7.40/1.30/1.30. This ratio is close to the proportions of CO7-HYB mixtures (7/1.5/1.5).

4.11.3 Optimal Mix Proportion Calculation for C$\bar{S}$ACO Paste

Similar to the previous calculations, CF_{CO} and $CF_{C\bar{S}A}$ were calculated as $-486W_{CO}$ and $580W_{C\bar{S}A}$, respectively. For C$\bar{S}$ACO mixture to provide zero carbon emission, the difference between CF_{CO} and $CF_{C\bar{S}A}$ was set to zero. The calculations yield a $W_{CO}/W_{C\bar{S}A}$ ratio of 580/486=1.19 (CO/DBM/C$\bar{S}$A≅5.44/0.00/4.56). Using more than 54.4 wt. % CO in C$\bar{S}$ACO pastes would lead to carbon-negative mixtures.

CHAPTER 5

CONCLUSIONS AND RECOMMENDATIONS

5.1 Conclusions

An attempt was made to produce magnesium oxalate cement by combining clay oxalate and dead-burned magnesia. Then, dead-burned magnesia was substituted with C$\overline{S}$A clinker to reduce the environmental impact of the mixtures. The following conclusions were drawn:

- A method to produce CO was developed. The reactivity of COC pastes increased with decreasing C/OA.
- A recipe to prepare COC with DBM or C$\overline{S}$A clinker (or with a combination of both) was developed. Making COC mortars with W/B=0.35 and S/B=2.5 resulted in workable mixtures, while W/B=0.30 works fine for paste making.
- Strength increased with increasing CO dosage up to 70 wt. % of the total powder content. CO7-DBM mixture gave the highest compressive strength at early and late ages, reaching 20 MPa only 6h after mixing and ~35 MPa at 28d. Increasing W/B caused a drop in strength. Furthermore, replacing DBM with C$\overline{S}$A clinker resulted in an overall decrease in strength. The decrease in the early strength was more significant than the late strength in the mixtures where DBM was substituted with C$\overline{S}$A. 28d strength of ~30 MPa was achieved for CO7-HYB and CO7-C$\overline{S}$A mortar specimens.
- Higher pH values are achieved in COC mixtures made with DBM.
- The setting takes longer with decreasing CO dosage. Incorporating C$\overline{S}$A clinker results in a warmer mixture and speeds up the setting significantly.
- Quartz coming from the clay was observed in XRD patterns of CO and COC pastes. Glushinskite was detected in COC paste powders incorporating DBM. Trace amounts of ettringite were found in COC pastes with C$\overline{S}$A clinker. The

hardened media of COC pastes are primarily composed of amorphous reaction products.

- The MIP results showed that the total porosity of COC pastes is less than that of Portland cement pastes and comparable to magnesium phosphate cement pastes.
- COC mortars lost ~30-40 % of their strength on the first day of water immersion. MCO and HYBCO mortars regained the lost strength in 28 days underwater, whereas C$\overline{S}$ACO mortar could not do so.
- Simple carbon footprint calculations yielded CO/DBM/C$\overline{S}$A ratios of 8.19/1.81/0.00, 7.40/1.30/1.30, and 5.44/0.00/4.56 to make carbon-neutral MCO, HYBCO, and C$\overline{S}$ACO pastes, respectively.
- The findings of this study suggest that COC mixtures made with CO/DBM/C$\overline{S}$A=7.40/1.30/1.30 can give medium strength, show sufficient resistance to water, and be carbon-neutral.

5.2 Recommendations for Future Studies

The subjects listed below could be potential research topics for developing clay oxalate cement:

- Investigation of the effect of the type of clay used and C/OA on the microstructure and performance of clay oxalate cement
- Investigation of the effect of retarder chemicals (e.g., borax) on setting time and fluidity of COC
- Investigation of the water resistance of COC mineralogically to understand the mechanism behind the strength regain of MCO and HYBCO mortar specimens

REFERENCES

Aitcin, P.-C. (2008). *Binders for Durable and Sustainable Concrete*. CRC Press. https://doi.org/10.1201/9781482265767

ASTM C109/C109M. (2020). *Standard Test Method for Compressive Strength of Hydraulic Cement Mortars (Using 2-in. or [50-mm] Cube Specimens)*. ASTM International, West Conshohocken, PA.

ASTM C305. (2020). *Standard Practice for Mechanical Mixing of Hydraulic Cement Pastes and Mortars of Plastic Consistency*. ASTM International, West Conshohocken, PA.

ASTM C807. (2021). *Standard Test Method for Time of Setting of Hydraulic Cement Mortar by Modified Vicat Needle*. ASTM International, West Conshohocken, PA.

Baumert, K. A., Herzogh, T., & Pershing, J. (2005). *Navigating the Numbers: Greenhouse Gas Data and International Climate Policy*. https://www.wri.org/research/navigating-numbers

Bernard, E., Lothenbach, B., Le Goff, F., Pochard, I. & Dauzères, A. (2017). Effect of magnesium on calcium silicate hydrate (C-S-H). *Cement and Concrete Research*, *97*, 61–72. https://doi.org/10.1016/j.cemconres.2017.03.012

Bilginer, B. A. (2018). *Development of Magnesium Potassium Phosphate Cement Pastes and Mortars Incorporating Fly Ash*. [Master's thesis, Middle East Technical University]. http://etd.lib.metu.edu.tr/upload/12622593/index.pdf

Brien, J. v., Henke, K. R., & Mahboub, K. C. (2013). Observations of peak strength behaviour in CSA cement mortars. *Journal of Green Building*, *8*(3), 97–115. https://doi.org/10.3992/jgb.8.3.97

Canbek, O. (2018). *Production of Low-Energy Cements Using Various Industrial Wastes*. [Master's thesis, Middle East Technical University]. http://etd.lib.metu.edu.tr/upload/12622661/index.pdf

Canbek, O., Shakouri, S., & Erdoğan, S. T. (2020). Laboratory production of calcium sulfoaluminate cements with high industrial waste content. *Cement and Concrete Composites*, *106*, 103475. https://doi.org/10.1016/j.cemconcomp.2019.103475

CEMBUREAU. (2022). *CEMBUREAU 2021 Activity Report*. https://cembureau.eu/media/03cgodyp/2021-activity-report.pdf

Curetti, N., Pastero, L., Bernasconi, D., Cotellucci, A., Corazzari, I., Archetti, M., & Pavese, A. (2022). Thermal stability of calcium oxalates from CO2 sequestration for storage purposes: An in-situ HT-XRPD and TGA combined study. *Minerals*, *12*(1). https://doi.org/10.3390/min12010053

Devasahayam, S., & Strezov, V. (2018). Thermal decomposition of magnesium carbonate with biomass and plastic wastes for simultaneous production of hydrogen and carbon avoidance. *Journal of Cleaner Production*, *174*, 1089–1095. https://doi.org/10.1016/j.jclepro.2017.11.017

Dong, H., Gao, P., & Ye, G. (2017). Characterization and comparison of capillary pore structures of digital cement pastes. *Materials and Structures*, *50*(2). https://doi.org/10.1617/s11527-017-1023-9

Erdoğan, S. T., Bilginer, B. A., & Canbek, O. (2022). Preparation and characterization of magnesium oxalate cement. *EngrXiv*. https://doi.org/10.31224/2298

Fukuhara, M., Goto, S., Asaga, K., Daimon, M., & Kondo, R. (1981). Mechanisms and kinetics of C4AF hydration with gypsum. *Cement and Concrete Research*, *11*(3), 407–414. https://doi.org/10.1016/0008-8846(81)90112-5

Gagg, C. R. (2014). Cement and concrete as an engineering material: An historic appraisal and case study analysis. *Engineering Failure Analysis*, *40*, 114–140. https://doi.org/10.1016/j.engfailanal.2014.02.004

Gelli, R., Tonelli, M., Martini, F., Calucci, L., Borsacchi, S., & Ridi, F. (2022). Effect of borax on the hydration and setting of magnesium phosphate cements. *Construction and Building Materials*, *348*, 128686. https://doi.org/10.1016/j.conbuildmat.2022.128686

Gražulis, S., Chateigner, D., Downs, R. T., Yokochi, A. F. T., Quirós, M., Lutterotti, L., Manakova, E., Butkus, J., Moeck, P., & le Bail, A. (2009). Crystallography Open Database – an open-access collection of crystal structures. *Journal of Applied Crystallography*, *42*(4), 726–729. https://doi.org/10.1107/S0021889809016690

Gražulis, S., Daškevič, A., Merkys, A., Chateigner, D., Lutterotti, L., Quirós, M., Serebryanaya, N. R., Moeck, P., Downs, R. T., & le Bail, A. (2012). Crystallography Open Database (COD): an open-access collection of crystal structures and platform for world-wide collaboration. *Nucleic Acids Research*, *40*(D1), D420–D427. https://doi.org/10.1093/nar/gkr900

Hanein, T., Galvez-Martos, J.-L., & Bannerman, M. N. (2018). Carbon footprint of calcium sulfoaluminate clinker production. *Journal of Cleaner Production*, *172*, 2278–2287. https://doi.org/10.1016/j.jclepro.2017.11.183

İçinsel, N. (2020). *Development of Magnesium Oxalate Cements with Recycled Portland Cement Paste*. [Master's thesis, Middle East Technical University]. http://etd.lib.metu.edu.tr/upload/12625902/index.pdf

Ivandini, T. A., Rao, T. N., Fujishima, A., & Einaga, Y. (2006). Electrochemical oxidation of oxalic acid at highly boron-doped diamond electrodes. *Analytical Chemistry*, *78*(10), 3467–3471. https://doi.org/10.1021/ac052029x

Jahren, P., & Sui, T. (2013). *Concrete and Sustainability*. CRC Press. https://doi.org/10.1201/b15160

Kawai, E., Ozawa, A., & Leibowicz, B. D. (2022). Role of carbon capture and utilization (CCU) for decarbonization of industrial sector: A case study of Japan. *Applied Energy*, *328*, 120183. https://doi.org/10.1016/j.apenergy.2022.120183

Kumar, R., & Bhattacharjee, B. (2004). Assessment of permeation quality of concrete through mercury intrusion porosimetry. *Cement and Concrete Research*, *34*(2), 321–328. https://doi.org/10.1016/j.cemconres.2003.08.013

Le Rouzic, M., Chaussadent, T., Platret, G., & Stefan, L. (2017). Mechanisms of k-struvite formation in magnesium phosphate cements. *Cement and Concrete Research*, *91*, 117–122. https://doi.org/10.1016/j.cemconres.2016.11.008

Luo, Z., Ma, Y., He, H., Mu, W., Zhou, X., Liao, W., & Ma, H. (2021). Preparation and characterization of ferrous oxalate cement—A novel acid-base cement. *Journal of the American Ceramic Society*, *104*(2), 1120–1131. https://doi.org/10.1111/jace.17511

Mastuli, M. S., Kamarulzaman, N., Nawawi, M. A., Mahat, A. M., Rusdi, R., & Kamarudin, N. (2014). Growth mechanisms of MgO nanocrystals via a sol-gel synthesis using different complexing agents. *Nanoscale Research Letters*, *9*(1), 134. https://doi.org/10.1186/1556-276X-9-134

Monteiro, P., Miller, S., & Horvath, A. (2017). Towards sustainable concrete. *Nature Materials*, *16*, 698–699. https://doi.org/10.1038/nmat4930

Nobre, J., Hawreen, A., Bravo, M., Evangelista, L., & de Brito, J. (2020). Magnesia (MgO) production and characterization, and its influence on the performance of cementitious materials: A review. In *Materials* (Vol. 13, Issue 21, pp. 1–31). MDPI AG. https://doi.org/10.3390/ma13214752

Odler, I. (2000). *Special Inorganic Cements*. E & FN Spon. https://doi.org/10.1201/9781482271942

Peñaloza Isidro, L. K., Ortiz Rodriguez, O. O., & Sánchez Molina, J. (2018). Study of the carbon footprint in a ceramic production process in the metropolitan area of Cucuta. *Respuestas*, *23*(2), 89–95. https://doi.org/10.22463/0122820X.1741

Prosser, H. J., & Wilson, A. D. (1986). Development of materials based on acid-base reaction cements. *Materials & Design*, *7*(5), 262–266. https://doi.org/10.1016/0261-3069(86)90052-X

Schuler, E., Demetriou, M., Shiju, N. R., & Gruter, G. J. M. (2021). Towards Sustainable Oxalic Acid from CO2 and Biomass. In *ChemSusChem* (Vol. 14, Issue 18, pp. 3636–3664). John Wiley and Sons Inc. https://doi.org/10.1002/cssc.202101272

Scrivener, K., Snellings, R., & Lothenbach, B. (2016). *A Practical Guide to Microstructural Analysis of Cementitious Materials*. CRC Press. https://doi.org/10.1201/b19074

Shand, M. A. (2006). *The Chemistry and Technology of Magnesia*. John Wiley & Sons, Inc. https://doi.org/10.1002/0471980579

Shand, M. A., Al-Tabbaa, Abir., Qian, Jueshi., Mo, Liwu., & Jin, Fei. (2020). *Magnesia cements : from formulation to application*. Elsevier. https://doi.org/10.1016/C2010-0-68998-X

Sharp, J. H., Lawrence, C. D., & Yang, R. (1999). Calcium sulfoaluminate cements—low-energy cements, special cements or what? *Advances in Cement Research*, *11*(1), 3–13. https://doi.org/10.1680/adcr.1999.11.1.3

Tan, Y., Yu, H., Li, Y., Bi, W., & Yao, X. (2016). The effect of slag on the properties of magnesium potassium phosphate cement. *Construction and Building Materials*, *126*, 313–320. https://doi.org/10.1016/j.conbuildmat.2016.09.041

TS EN 196-1. (2016). *Methods of testing cement - Part 1: Determination of strength*. Turkish Standards Institution.

USGS. (2022). *2018 Mineral Yearbook - Magnesium Compounds (Advance Release)*. https://pubs.usgs.gov/myb/vol1/2018/myb1-2018-magnesium-comp.pdf

Wagh, A. S. (2016). *Chemically Bonded Phosphate Ceramics* (2nd ed.). Elsevier. https://doi.org/10.1016/C2014-0-02562-2

Wagh, A. S., & Jeong, S. Y. (2003). Chemically Bonded Phosphate Ceramics: I, A Dissolution Model of Formation. *Journal of the American Ceramic Society*, *86*(11), 1838–1844. https://doi.org/10.1111/j.1151-2916.2003.tb03569.x

Walling, S. A., & Provis, J. L. (2016). Magnesia-Based Cements: A Journey of 150 Years, and Cements for the Future? In *Chemical Reviews* (Vol. 116, Issue 7, pp. 4170–4204). American Chemical Society. https://doi.org/10.1021/acs.chemrev.5b00463

Wilson, A. D., & Nicholson, J. W. (1993). *Acid-Base Cements*. Cambridge University Press. https://doi.org/10.1017/CBO9780511524813

Xu, B., Ma, H., Shao, H., Li, Z., & Lothenbach, B. (2017). Influence of fly ash on compressive strength and micro-characteristics of magnesium potassium phosphate cement mortars. *Cement and Concrete Research*, *99*, 86–94. https://doi.org/10.1016/j.cemconres.2017.05.008

Yang, J., & Qian, C. (2010). Effect of borax on hydration and hardening properties of magnesium and pottassium phosphate cement pastes. *Journal of Wuhan University of Technology-Mater. Sci. Ed.*, *25*(4), 613–618. https://doi.org/10.1007/s11595-010-0055-6

Yong-xin, L., Yi-min, C., Hong-tao, Z., Xing-yang, H., Jiang-xiong, W., & Wen-sheng, Z. (2003). Microstructure and composition of hydration products of ordinary Portland cement with ground steel-making slag. *Journal of Wuhan University of Technology-Mater. Sci. Ed.*, *18*(4), 76–79. https://doi.org/10.1007/BF02838398

Yuan, Q., Liu, Z., Zheng, K., & Ma, C. (2021). Inorganic cementing materials. In *Civil Engineering Materials* (pp. 17–57). Elsevier. https://doi.org/10.1016/B978-0-12-822865-4.00002-7

Zeng, Q., Li, K., Fen-Chong, T., & Dangla, P. (2012). Analysis of pore structure, contact angle and pore entrapment of blended cement pastes from mercury porosimetry data. *Cement and Concrete Composites*, *34*(9), 1053–1060. https://doi.org/10.1016/j.cemconcomp.2012.06.005

Zhao, L., Feng, J., & Dong, H. (2022). Analysis of carbon footprint and reduction approach of magnesia production in China. *Journal of Cleaner Production*, *334*, 130194. https://doi.org/10.1016/j.jclepro.2021.130194